

1 **Paleocene-Eocene age glendonites from the Mid-Norwegian Margin**

2 **- Indicators of cold snaps in the hothouse?**

3 Madeleine L. Vickers^{1*}, Morgan T. Jones¹, Jack Longman², David Evans^{3,4,†}, Clemens V. Ullmann⁵, Ella
4 Wulfsberg Stokke¹, Martin Vickers⁶, Joost Frieling⁷, Dustin T. Harper⁸, Vincent J. Clementi⁹ & IODP
5 Expedition 396 Scientists¹⁰

6 ¹ Centre for Planetary Habitability (PHAB), University of Oslo, P.O. Box 1028 Blindern, 0315 Oslo, Norway

7 ² Department of Geography and Environmental Sciences, Northumbria University, Newcastle-upon-Tyne, UK

8 ³ Institute of Geosciences, Goethe University Frankfurt, Altenhöferallee 1, 60438 Frankfurt am Main, Germany

9 ⁴ FIERCE, Frankfurt Isotope & Element Research Center, Goethe University Frankfurt, Altenhöferallee 1, 60438 Frankfurt am
10 Main, Germany

11 ⁵ Camborne School of Mines, University of Exeter, Penryn Campus, Penryn TR10 9FE, UK

12 ⁶ Department of Chemistry, UCL, 20 Gordon Street, London WC1H 0AJ, UK

13 ⁷ Department of Earth Sciences, University of Oxford, Oxford, United Kingdom

14 ⁸ University of Utah, Dept. of Geology & Geophysics, 115 S 1460 E, Salt Lake City, UT 84112, U.S.A.

15 ⁹ Department of Marine and Coastal Sciences, Rutgers University, New Brunswick, NJ 08901, U.S.A.

16 ¹⁰International Ocean Discovery Program, Texas A&M University, College Station TX 77845 U.S.A. Email:
17 Expedition_396_Participants@iodp.tamu.edu

18 *m.l.vickers@geo.uio.no

19 [†] Now at: School of Ocean and Earth Science, University of Southampton, Southampton, SO14 3ZH, UK

20 **Keywords:** PETM; ikaite; Paleogene; International Ocean Discovery Program (IODP); JOIDES
21 Resolution; Expedition 396; Sites U1567, U1568, U1569, U1570.

22 **Abstract**

23 The International Ocean Discovery Program (IODP) Expedition 396 to the mid-Norwegian margin
24 recovered >1300 m of pristinely preserved, volcanic ash-rich sediments deposited during the late
25 Paleocene and early Eocene, from close to the centre of the North Atlantic Igneous Province (NAIP).

26 Remarkably, many of these cores contain glendonites, pseudomorphs after the purported cold-water
27 mineral ikaite, from sediments dated to the late Paleocene and early Eocene. These time intervals
28 span some of the hottest climates of the Cenozoic, including the Paleocene-Eocene Thermal Maximum
29 (PETM). Global deep ocean temperatures are not thought to have dropped below 10 °C at any point
30 during this time, making the occurrence of supposedly cold-water (near-freezing temperature)
31 glendonite pseudomorphs seemingly paradoxical. This study presents a detailed sedimentological,
32 geochemical, and microscopic study of the IODP Exp. 396 glendonites, and presents an updated model
33 for the ikaite-to-calcite transformation for these glendonites. Specifically, we show that early
34 diagenesis of basaltic ashes of the NAIP appear to have chemically promoted ikaite growth in the
35 sediments in this region. Together with existing knowledge of late Paleocene and early Eocene
36 glendonites from Svalbard to the north, and early Eocene glendonites from Denmark to the south,
37 these new glendonite finds possibly imply episodic, short-duration, and likely localised cooling in the
38 Nordic Seas region, which may have been directly or indirectly linked to the emplacement of the NAIP.

39 **1. Introduction**

40 Glendonites are pseudomorphs after the mineral ikaite, a metastable, hydrated form of calcium
41 carbonate ($\text{CaCO}_3 \cdot 6\text{H}_2\text{O}$), which is found today growing in a range of environments (alkaline lakes, sea
42 ice, concrete, in estuarine settings, deep marine sediments and more; Council and Bennet, 1993;
43 Buchardt et al., 2001; Dieckmann et al., 2008; Boch et al., 2015; Zhou et al., 2015; Schultz et al., 2022;
44 2023a). Certain physical and chemical conditions are necessary in order for ikaite to precipitate
45 preferentially over the more stable anhydrous CaCO_3 polymorphs (calcite, aragonite, vaterite). These
46 parameters may include low temperatures, high alkalinity, and a range of possible chemical inhibitors
47 of the anhydrous polymorphs (e.g. high aqueous Mg, phosphate, and/or sulphate concentrations;
48 certain dissolved organic compounds) (Council and Bennett, 1993; Buchardt et al., 2001; Zhou et al.,
49 2015; Purgstaller et al., 2017; Stockmann et al., 2018; Whiticar et al., 2022). Whilst laboratory studies
50 have successfully, if fleetingly, precipitated ikaite at warm temperatures (≤ 35 °C), cold water
51 temperatures (< 10 °C) are much more favourable for the precipitation, growth, and longevity of this
52 mineral (Purgstaller et al., 2017; Stockmann et al., 2018; Tollefsen et al., 2020; Vickers et al., 2022). In
53 nature, ikaite has not been discovered growing above 7 °C (Suess et al., 1982; Dieckmann et al., 2008;
54 Zhou et al., 2015; Boch et al., 2015; Stockmann et al., 2022).

55 Glendonites are found throughout the geological record in marine sedimentary settings, sometimes
56 associated with glacial deposits (e.g. Kemper, 1987; Alley et al., 2020), in sediments deposited during
57 periods of both icehouse and greenhouse climate (Rogov et al., 2021; 2023). The occurrence of

58 glendonites in Mesozoic marine sediments has fuelled the debate about whether ephemeral polar ice
59 sheets waxed and waned during this long-term global greenhouse climate (e.g. Kemper, 1987; de Lurio
60 and Frakes, 1999; Rogov et al., 2017; Vickers et al., 2019; Merkel and Munnecke, 2023). Across the
61 Cenozoic sedimentary record, glendonites are found at increasingly broader latitude ranges through
62 time, coincident with the growth of polar ice caps and global climate cooling (Rogov et al., 2021).
63 However, reports of glendonites – including the largest ever discovered on Earth – from successions
64 deposited in the Nordic Seas region during the early Paleogene greenhouse have been a topic of
65 controversy in the paleoclimate community due to the apparent mismatch with concurrent
66 paleotemperature proxies (Huggett et al., 2005; Spielhagen and Tripathi, 2009). Deep ocean bottom
67 water temperatures were $>10\text{ }^{\circ}\text{C}$ across the globe, including the North Atlantic, during much of the
68 Paleocene and Early Eocene (Zachos et al., 2008; Dunkley-Jones et al., 2013; Westerhold et al., 2020;
69 Meckler et al. 2022), such that the presence of glendonites in marine sedimentary sequences during
70 this time appears paradoxical. Whilst the successful synthesis of ikaite at warm ($\leq 35\text{ }^{\circ}\text{C}$) temperatures
71 in laboratory conditions raises the possibility of ikaite/glendonite formation at much warmer
72 temperatures than modern-day natural ikaites (Purgstaller et al., 2017; Tollefsen et al., 2020), the
73 conditions under which this was achieved in the laboratory are unlike marine natural settings (e.g.,
74 compared to modern marine ikaite-bearing sites those precipitation experiments were characterised
75 by DIC concentrations at least an order of magnitude higher than typical pore water profiles and Ω_{calcite}
76 >100 , far in excess of that typically found in natural settings; Zhou et al., 2015).

77 In addition, clumped isotope temperature reconstructions for ikaite precipitation/transformation
78 temperatures from a Danish early Eocene succession suggest cold formation (or perhaps
79 transformation) conditions ($0 - 9\text{ }^{\circ}\text{C}$) for the parent ikaite (Vickers et al., 2020). Given that the ikaite
80 minerals grew from pore waters in the shallow subsurface (e.g., Zhou et al., 2015; Schultz et al., 2022),
81 this suggests that local bottom water temperatures must have been at least this cold (Vickers et al.,
82 2020), since temperature increases with burial depth. Reconstructed sea surface temperatures from
83 biomarkers for the North Sea area (Denmark) also suggest that short-term cooling events of
84 magnitude c. $5 - 7\text{ }^{\circ}\text{C}$ (down to SSTs of $15\text{ }^{\circ}\text{C}$ or lower) may have punctuated the late Paleocene to
85 early Eocene (Stokke et al., 2020a; Vickers et al., 2020; summarised by Jones et al., 2023). While the
86 potential drivers of intermittent cooling episodes have been touched upon by previous studies
87 (Schoon et al., 2015; Stokke et al., 2020a; Vickers et al., 2020), the causes, spatial extent, and
88 recurrence times of such events remains unresolved.

89 The International Ocean Discovery Program (IODP) Expedition 396 to the Norwegian continental
90 margin (August – September 2021) recovered numerous glendonites in ash-bearing deposits dated

91 as latest Paleocene and earliest Eocene, including within those sediments deposited during the
92 Paleocene-Eocene Thermal Maximum (PETM) hyperthermal event (Berndt et al., 2023; Planke et al.,
93 2023a). Deep ocean bottom water temperatures may have reached 15 °C or more during the 150 –
94 200 kyr-long PETM hyperthermal (Röhl et al., 2007; Zachos et al., 2008; Murphy et al., 2010; Dunkley
95 Jones et al., 2013; Westerhold et al., 2020). This makes the discovery of pseudomorphs after a mineral
96 favoured by near-freezing conditions in shallow epicontinental seas truly remarkable if the age of their
97 formation and recrystallisation coincided with the depositional age of the host sediments. If the parent
98 ikaite grew during the PETM or the hothouse earliest Eocene climate (as was the case for the well-
99 studied Fur Formation glendonites; Vickers et al., 2020), this raises questions about regional seaway
100 connectivity and stratification in the Nordic Seas, as an extreme thermocline within these shallow seas
101 is one way to reconcile cold bottom water and warm surface water proxies. The presence of
102 glendonites in Nordic Seas strata could imply that current global and regional temperature
103 reconstructions based on biogenic carbonates and lipid biomarkers do not represent the full spectrum
104 of climate variability in the early Paleogene Northern Hemisphere.

105 This study documents and describes the glendonites recovered from IODP Exp. 396 cores and their
106 stratigraphic distribution, using microscopic and geochemical analyses along with sedimentological
107 data to elucidate the timing, climate, and chemical regimes that facilitated their formation.

108 **2. Materials and Methods**

109 *2.1 Geological setting and sampling*

110 IODP Expedition 396 drilled 21 boreholes along the mid-Norwegian continental margin during August
111 and September 2021, recovering igneous and sedimentary rocks ranging from lava flow fields to
112 hydrothermal vent complexes, including thick successions of upper Paleocene and lower Eocene strata
113 (Fig. 1A). Ship-board sedimentary logging was followed by a more detailed high-resolution study of
114 recovered cores stored at MARUM, Bremen, under refrigerated conditions (c. 4 °C). Paleocene-Eocene
115 sedimentary successions were cored along the Modgunn and Mimir transects (Fig. 1B and C).

116 Boreholes from the Modgunn transect (Sites U1567-U1568) span the crater of a Paleogene
117 hydrothermal vent complex close to the Vøring transform margin (Fig. 1B; Planke et al., 2023a,b).
118 These vents formed due to the violent expulsion of volatiles generated by contact metamorphism of
119 organic-rich sediments around igneous intrusions, and from magmatic degassing (e.g. Svensen et al.,
120 2004). The Modgunn crater is approximately 80 m deep compared to the paleo-seafloor, with a 200-
121 240m-wide feeder system that is rooted in a series of nested sill intrusions (Berndt et al., 2023). The

122 vent infill consists predominantly of laminated diatom-rich mud, mudstones, and ash layers that
123 rapidly accumulated to fill the bathymetric depression. The strata exhibit a negative $\delta^{13}\text{C}$ excursion
124 and the first and last occurrence of the biostratigraphic marker taxa *Apectodinium augustum* and
125 *Hemiaulus proteus* (Fig. 2). Based on these biostratigraphic and chemostratigraphic constraints,
126 Berndt et al. (2023) showed the vent formed just before the PETM onset and was completely filled
127 within the duration of the PETM CIE.

128 The Mimir High (Sites U1569-U1570) is a borehole transect through a marginal high on the Vøring
129 Transform Margin (Fig. 1C; Planke et al., 2023a,c). Uplift and erosion of the marginal high has removed
130 any basalt cover (Berndt et al., 2001), providing a window to access stratigraphic successions below
131 the breakup volcanism. The strata dip to the north, so a transect of boreholes was designed to provide
132 a composite late Paleocene – early Eocene section with overlap between each hole. These strata
133 consist of a mix of mud, mudstones, carbonates, igneous units, and ash layers (Planke et al., 2023a,c).
134 For three Holes (U1569A, U1570A and U1570D), on board biostratigraphy showed the presence of the
135 PETM-marker taxon *Apectodinium augustum* (Planke et al. 2023c) (Fig. 2).

136 Core sampling, including the collection of glendonites, was undertaken in April 2022 and high-
137 resolution sediment logging of the glendonite-bearing core sections was undertaken in August 2022,
138 at MARUM, University of Bremen, Germany.

139 At each hole, interstitial water (IW) samples were taken at intervals of ~3 m of sediment in the upper
140 50 m, ~1 sample every 9.5 m for the lower parts of the cored sediment. Standard IODP methods for
141 IW extraction were used at all sites. Following whole-core recovery to the catwalk, full round samples
142 were collected, sealed and transferred to the shipboard chemistry lab, where sediment exteriors were
143 carefully removed to reduce potential contamination from drilling fluids. The samples were
144 individually ‘squeezed’ - placed into a Carver press and subjected to 35,000 lb (15,875 kg) force.
145 Squeezed fluid was then filtered through a Whatman No. 1 filter (11 μm) and 0.5 mL was discarded.
146 The remaining fluids were collected in acid-cleaned syringes after filtering through 0.45 μm
147 polyethersulfone membranes, and split into aliquots. All analyses of the collected IWs were completed
148 following the standard shipboard methods of the R/V JOIDES Resolution (Planke et al., 2023d), and
149 are published in Planke et al. (2023a) and (2023b).

150 2.2 Carbon isotope analysis

151 A selection of bulk rock sub-samples were selected for carbon isotope analysis, in order to provide
152 new chemostratigraphic data for certain of the Mimir holes, and to complement the existing $\delta^{13}\text{C}_{\text{org}}$

153 dataset for the Modgunn transect (Berndt et al., 2023). Dried bulk rock samples were powdered and
154 decarbonated using 1 M HCl for 72 h, including a brief (c. 1 h) heating step at 50 °C during the
155 acidification process to remove any siderite that has been identified as occasionally present in these
156 sediments. The samples were then cleaned using deionised water and were oven dried at 50 °C before
157 being re-homogenised. Analyses of squeeze cake samples from the IW extraction procedure were
158 performed using a Thermo Fisher Scientific Flash Elemental Analyzer, coupled to a Thermo Fisher
159 Scientific DeltaV Isotope Ratio Mass Spectrometer at the CLIPT Lab, University of Oslo. An expanded
160 dataset from the samples collected in Bremen were analysed using a Thermo Fisher DeltaV Advantage
161 Mass Spectrometer at the School of Ocean & Earth Science & Technology (SOEST) at the University of
162 Hawaii at Mānoa. Each sample was run in duplicate to test reproducibility, which was < 0.06‰ for
163 both sample sets.

164 *2.3 Powder X-Ray Diffraction (PXRD)*

165 Powder X-ray diffraction (PXRD) was carried out on dried, powdered bulk sub-samples of five
166 glendonites from the Exp. 396 cores, using a Stoe StadiP transmission (thin-foil) diffractometer with a
167 copper anode at 30 mA, 40 kV and a germanium 111 monochromator to produce $K\alpha_1$ X-rays. The
168 diffracted beam was collected by an 18° 2 θ Dectris Mythen1K silicon strip detector. Samples were
169 sandwiched between two thin cellulose acetate discs and mounted in a holder set to spin continuously
170 during data collection. Data sets were scanned from 5 to 65° 2 θ stepping at 0.5° and 20 s/step. The
171 resultant raw data has a step of 0.015° 2 θ . Machine alignment was monitored using an NBS silicon
172 standard. Phase analysis was undertaken using Bruker's 'Eva' program (Gates-Rector and Blanton,
173 2019) interfaced with the Powder Diffraction File provided by the International Centre for Diffraction
174 Data.

175 *2.4 Microscopy*

176 Four polished thin sections were made from three glendonites (those in Cores U1569A-19R-2,
177 U1570A-15R-1, and U1567C-11X-1), and examined using a light microscope to compare to published
178 data on glendonite microfabric and look for different carbonate growth phases. A Hitachi SU5000 FE-
179 SEM, equipped with a Bruker EDS was used to examine porosity and spatial chemical variation across
180 the sub-samples.

181 *2.5 Laser Ablation Inductively Coupled Plasma Mass Spectrometry (LA ICP-MS)*

182 Laser ablation trace element analyses were performed on polished thin sections of glendonites from
183 Cores U1569A-19R-2, U1570A-15R-1, and U1567C-11X-1 at the Frankfurt Isotope and Element

184 Research Center (FIERCE) in the Institute of Geosciences at Goethe University Frankfurt. Different
185 carbonate phases were targeted. The system features a 193 nm RESOLUTION M-50 laser ablation (LA)
186 system with two-volume LaurinTechnic ablation cell connected to a ThermoScientific Element XR
187 sector field inductively coupled plasma mass spectrometer (ICP-MS). All analyses were performed as
188 'spot' measurements, utilising relatively low repetition rates to ablate through the thin sections
189 analysed here. Ablation took place with He in the outer cell (400 ml/min) and Ar sample gas from the
190 ICP-MS (1.025 l/min) mixed into the lower-volume inner cell. N₂ was admixed downstream of the
191 ablation cell (4.5 ml/min) to improve sensitivity (e.g. Durrant, 1994). The ICP-MS was fitted with a Ni
192 jet sample cone and Ni H skimmer cone and operated in medium resolution mode. Tuning of the
193 system was performed to maximise sensitivity (~6 M cps ²³⁸U in low resolution mode; NIST SRM612
194 60 μm, 6 Hz, 6 J/cm²) while maintaining the oxide and doubly charged production rate below 0.5% and
195 2% respectively. Monitored masses included ¹¹B, ²³Na, ²⁴Mg, ²⁵Mg, ²⁷Al, ³⁹K, ⁵⁵Mn, ⁵⁶Fe, ⁸⁸Sr, ¹³⁸Ba, ²⁰⁸Pb,
196 and ²³⁸U.

197 Samples were ablated using a 50 μm diameter laser beam at 4 Hz with an on-sample fluence of 5
198 J/cm². Quantification was performed using ⁴³Ca as the internal standard and NIST SRM610 as the
199 external standard. Data processing was performed using an in-house Matlab script following
200 established procedures (Heinrich et al., 2003), described in detail elsewhere (Evans and Müller, 2018).
201 Briefly: all analyses were baseline corrected by subtracting the mean of the two adjacent gas-blank
202 datasets, normalised to ⁴³Ca, and standardised into element/Ca molar ratios using the analyte/⁴³Ca
203 count/concentration ratio from NIST SRM610. No significant drift in this count ratio was observed for
204 any relevant analyte for the session reported here such that standardisation was based on the mean
205 of all available NIST analyses. Down-hole elemental fractionation relative to Ca was corrected by
206 calculating least-squares 3rd-order polynomials through the NIST SRM610 element/⁴³Ca-depth data,
207 which were then used as the sweep-time specific ratios for sample quantification. The NIST SRM610
208 values of Jochum et al. (2011) were used in all cases except Mg, for which we use that of Pearce et al.
209 (1997) following the data analysis of Evans and Müller (2018).

210 Data quality was assessed via repeat analysis of the 'nanopellet' version of the CaCO₃ standards JcP-1
211 and MACS-3 (Garbe-Schönberg and Müller, 2014; Jochum et al., 2019), ablated in an identical manner
212 to the samples. Pooling together all analyses on both standards (n = 20) and comparing to the reported
213 values of Jochum et al. (2019) yields an accuracy of <5% for ¹¹B, ⁵⁶Fe, ⁸⁸Sr, <10% for ²³Na, ²⁴⁺²⁵Mg, ¹³⁸Ba,
214 ²³⁸U, 25% for ²⁷Al, 30% for ³⁹K, and 70% in the case of ⁵⁵Mn, comparable to the achievable long-term
215 data quality from a similar system (Evans and Müller, 2018, albeit using a quadrupole ICP-MS).
216 Precision (repeatability), defined as the 2SD of all individual analyses normalised to the reported value

217 was better than 10% in the case of ^{11}B , ^{23}Na , ^{88}Sr , ^{238}U , <15% for $^{24+25}\text{Mg}$, ^{39}K , ^{56}Fe , ^{138}Ba , 45% for ^{27}Al ,
218 and 130% for ^{55}Mn . We stress that all of these values are strongly concentration-dependent and may
219 under/overestimate sample data quality depending on the analyte concentration of a given sample
220 analysis.

221 *2.6 Inductively Coupled Plasma Optical Emission Spectrometry (ICP-OES)*

222 Minor element analyses for Mg, Sr, Na, Mn, Fe, S, P, Al and Rb were undertaken on selected
223 subsamples of dried, powdered, bulk glendonites using an Agilent 5110 VDV ICP-OES at the Camborne
224 School of Mines, University of Exeter, following the method detailed in Ullmann et al. (2020). The
225 minor element data are expressed as ratios to Ca and calibrated using certified single-element
226 standards mixed to match the chemical composition of the analysed samples. Precision and accuracy
227 of the analyses were measured and controlled by interspersing multiple measurements of
228 international reference materials, JLS-1 and quality control solutions (BCQ2 and BCQ3). Analytical
229 uncertainty of element/Ca ratios in these reference materials is less than 1 % (2 RSD) at concentrations
230 > 100 times the quantification limit (measured as 6 SD of the variability of blank solutions in a batch
231 run, $n = 5$). For lower concentrations, the uncertainty of individual measurements is similar to the
232 quantification limit, i.e. 6 $\mu\text{mol/mol}$ for Mg/Ca, 0.2 $\mu\text{mol/mol}$ for Sr/Ca, 0.02 mmol/mol for Na/Ca, 5
233 $\mu\text{mol/mol}$ for Mn/Ca, 5 $\mu\text{mol/mol}$ for Fe/Ca, 0.2 mmol/mol for S/Ca, 0.08 mmol/mol for P/Ca, 0.06
234 mmol/mol for Al/Ca, and 0.04 mmol/mol for Rb/Ca.

235 *2.7 Microprobe data, IODP Exp. 396 ashes*

236 A representative selection ($n=13$) of Exp. 396 ashes from Holes U1567A, U1567C, U1568A, U1568B,
237 U1569A, and U1570D were analysed for their major element composition. Individual silicate glass
238 grains were picked and mounted in epoxy for matrix glass analysis. Polished and carbon coated grain
239 mounts were analysed on a Cameca SX100 electron microprobe with 5 wavelength dispersive
240 spectrometers (WDS) at University of Oslo. Analyses were conducted with an accelerating voltage of
241 15 kV and a 10 nA beam current using a defocused beam size of 10 μm . Counting times were 10 s for
242 Na, Si, Cl, K, S, Fe, Al, Mg, and Mn; and 20 for Ca and Ti.

243 *2.8 PHREEQC modelling*

244 The PHREEQC model (version 3; Parkhurst and Appelo, 2013, using the phreeqc.dat database) was
245 used to calculate pore water chemical speciation and saturation indices for Hole U1568A, based on
246 multiple shipboard analyses of interstitial water (Planke et al., 2023a,b). The model input values were
247 those from the ICP-AES for consistency. The *in situ* pressures (in atm; 1 atm = 101 kPa) were estimated

248 using the measured water depth of 1707.4 m below surface (mbsf) and a pressure gradient of 0.1
249 atm/m in the water column. In the subsurface, a pressure gradient of 0.2 atm/m was assumed, giving
250 a pressure of 209 atm at the deepest interstitial water sample depth (192.4 m). The PHREEQC model
251 was run as a batch reactor for each solution using a table input into SOLUTION_SPREAD, then a second
252 simulation RUN_CELLS to recalibrate the pe and pH from the ionic balance of the shipboard
253 measurements of cation and anion contents (Planke et al., 2023b,c).

254 **3. Results**

255 *3.1 Sedimentological context*

256 The glendonites discovered by IODP Expedition 396 are found within two holes of the Modgunn
257 transect, U1567C (3°3.219'E 65°21.785'N) and U1568A (3°3.109'E 65°21.594'N); and within two holes
258 of the Mimir transect, U1569A (2°1.608'E 65°49.878'N) and U1570A (1°59.623'E 65°49.890'N) (Fig. 2
259 and Table 1). For the Modgunn transect, the glendonites are all found within the latest Paleocene and
260 PETM-aged hydrothermal vent infilling deposits (Unit IV, Fig. 2), in horizons with the most numerous
261 and thickest ash intervals (Fig. 2). Lithological Unit IV is described as “Dark greenish grey to very dark
262 grey claystone to siltstone, with common volcanic ash beds and light bioturbation” (Planke et al.,
263 2023b, p.10). The glendonites in the Mimir cores are found in early Eocene-aged parts of the
264 succession, in Unit Va and Vb of Hole U1570A, also in close association with numerous and thick ash
265 layers. In Hole U1569A the glendonites are found at the very top of Unit Va, some 17 m above the
266 thickest and most numerous ash horizons, although notably in an interval with limited core recovery
267 (Fig. 2), which implies that these sediments may be extremely rich with unconsolidated ash horizons.
268 The deposits of Lithological Unit Va are described as “very dark grey mudstone with sparse parallel
269 lamination and slight bioturbation, with rare limestone intervals and common ash beds”; and those of
270 Vb as “very dark grey mudstone with sparse parallel lamination and slight bioturbation, with common
271 ash beds and diagenetic pyrite.” (Planke et al., 2023c, p10 Sites U1569 & U1570). High-resolution logs
272 (5-cm scale) of the glendonite-bearing core sections and photographs of the *in situ* glendonites can be
273 found in the Supplementary Material.

274 *3.2 Organic carbon isotopes*

275 Organic carbon isotope data for the Mimir High (Holes U1570D, U1570A and U1569A) are shown on
276 Fig 2A. The carbon isotope data for the Modgunn hydrothermal vent complex is shown in Fig. 2B,
277 which includes new data from Hole U1568A and published data from Holes U1568B, U1567B, and
278 U1567C (Berndt et al., 2023). In the Modgunn boreholes, the PETM CIE is manifest as a negative CIE

279 of over 5 ‰ in Holes U1568A, U1567B, and U1567C, followed by a relaxation of $\delta^{13}\text{C}$ values back to c.
280 -1 ‰ compared to pre-PETM conditions for the rest of the vent infill. Hole U1568B currently has too
281 low data resolution, and Hole U1567A had extremely poor core recovery across the vent interval (Fig.
282 2B). The unusual PETM CIE shape at these localities is attributed to a change in the dominant carbon
283 source from terrestrial to marine-dominated organic matter into the extreme excursion and back to
284 terrestrially dominated organic matter for the minor excursion (Berndt et al., 2023). A similar CIE
285 shape has been observed nearby in the Grane field in the northern North Sea (Jones et al., 2019),
286 suggesting comparable paleoenvironmental conditions across the central part of the Nordic Seas area
287 at this time. The Mimir $\delta^{13}\text{C}_{\text{Org}}$ data spans the PETM interval in the three cores, identified by the first
288 and last occurrences of *A. augustum* (Planke et al., 2023c). There is only a slight (1-2 ‰) $\delta^{13}\text{C}_{\text{Org}}$
289 excursion is present in these holes, and it is difficult to differentiate between PETM and pre/post-
290 PETM strata on carbon isotopic evidence alone. The marine organic matter-rich CIE (~5 ‰) observed
291 at Modgunn and Grane has not been identified at Mimir from this dataset, but for Hole U1569A this
292 may be because there was poor core recovery over the critical PETM onset interval and the most
293 negative part of the CIE may be missing (Fig. 2A).

294 3.3 Glendonite morphology

295 The glendonites are variable in size and appearance, with some being cemented or partially cemented
296 (Fig. 3C, E, H and I), and some present as an uncemented amalgam of smaller crystals (Fig. 3B, D, F, G),
297 and some retaining their structure but as a porous mesh of calcite (Fig. 3A and J). In size, they range
298 from small fragments (2 – 5 mm across, Fig. 3A,D,F,I,J) to crystals up to or beyond the than the entire
299 width of the core (Fig. 3B,C) In some cases, the crystal appears to have grown over and incorporated
300 parts of the host sediment (Fig. 3E,H), yet in others appears to have either displaced the sediment it
301 was growing in (Fig. 3G), or grew up into the water column with later sedimentation burying it (Fig.
302 3C). Nearly all the recorded glendonite specimens can be ascribed to a single rosette morphotype (Fig.
303 3) (following terminology proposed by Frank et al., 2008), except for specimens from Fig. 3D, F, I and
304 J, in which the morphology is unclear due to the fragmented nature or disturbance of the structure
305 during drilling. They are generally pale beige to brown in colour, although cemented examples show
306 distinct areas within a cut 'crystal' of grey or white-pale brown carbonate (Fig. 3C,H). Some samples
307 are only small fragments of glendonite, identified by their characteristic bladed shape (e.g. Fig. 3A,E)
308 and/or the open, porous texture of the carbonate (e.g. Fig. 3F, I, J). Most of the glendonites are found
309 *in situ*, with the exception of sample U1567C-10X-3 40-45, where glendonite fragments were
310 identified entrained in the drill mud (Fig. 3A). Therefore, these fragments could have originated from

311 some short distance away from their final position within the core, likely the large glendonite found
312 in the core below (sample U1567C-11X-1 83-93; Fig. 3B).

313 3.4 PXRD

314 The PXRD analysis of the bulk composition of 5 different glendonites reveal that the glendonites are
315 mostly composed of calcite with a major to minor magnesian calcite component. Minor amounts of
316 quartz, halite, rhodochrosite (MnCO_3) and gypsum were also identified (Table 1 and Supplementary
317 Material Fig. S11).

318 3.5 Microscopy

319 Polished thin sections were examined by light microscopy and revealed several different carbonate
320 phases (Figs. 4 and 5). These have been grouped by appearance (colour, texture, relationship to other
321 phases) and geochemistry, and are described in detail in Table 2. Where possible, these phase names
322 are in keeping with previous studies' description of ikaite carbonate phases (e.g. Huggett et al., 2005;
323 Grasby et al., 2016; Vickers et al., 2018; Mikhailova et al., 2021; Scheller et al., 2021; Schultz et al.,
324 2023a; Counts et al., *accepted*)., with the main phase type assigned based on colour and sub-types
325 based on microstructure and geochemical data.

326 3.6 LA ICP-MS

327 The LA ICP-MS trace element data shows that Mg/Ca ratios are distinct on average between the
328 carbonate phases, with $\text{Type 1A} \leq \text{1B} \leq \text{2A} = \text{2B} \leq 0$, albeit with substantial heterogeneity within a
329 phase such that the ranges overlap in most cases (Fig. 6). There is also substantial overlap between
330 types 1 and 2 for all other measured elemental ratios (Fe/Ca, Mn/Ca, Sr/Ca, P/Ca, S/Ca; Fig. 6). The
331 measurements made from the outer hard crust of the glendonite sample from core U1569A-19R-2
332 show the highest Mg/Ca contents of all, and distinctly higher S/Ca than all other carbonate phases.
333 Type 0 has significantly higher Mn/Ca and P/Ca than all other measured calcite phases, and
334 significantly lower S/Ca than other measured carbonate phases (Fig. 6).

335 3.7 ICP-OES

336 Bulk drill-sampled ICP-OES results find that the Exp. 396 glendonites have Mg/Ca ratios in the range
337 of c. 20 - 50 mmol/mol, comparable to the Fur Formation carbonates (Fig 7). Sr/Ca range from 1.5 -
338 1.8 mmol/mol; Fe/Ca from 1.6 - 38 mmol/mol, with an outlier of 165 mmol/mol (1568A 15X 4 55-58);

339 Mn/Ca ratios range from 0.4 - 8.4; P/Ca ratios range from 1.5 - 12.8 mmol/mol; and S/Ca ratios range
340 from 0.8 - 5.5 mmol/mol (Fig. 7).

341 *3.8 Microprobe data, 396 ashes*

342 The Exp. 396 ashes all have a basaltic tholeiitic composition, similar to the Fur positive series ashes
343 (Fig. 8). However, they have relatively high MgO content ranging from 4.3 to 9.6 wt%, which is
344 generally higher than that of the Fur positive series (3.3-7.1 wt%; Larsen et al., 2003; Stokke et al.,
345 2020b).

346 *3.9 IW analysis and PHREEQC modelling*

347 The shipboard analyses of IW samples showed non-typical behaviour within Units IV and V (the vent
348 infill) at Site 1568A, with lower alkalinity (2–3 mM) and higher pH (~8.2) compared to both underlying
349 and overlying strata (Planke et al., 2023b). Many IW profiles in ocean sediments above igneous
350 basement show a marked reduction in dissolved Mg/Ca ratios with depth (e.g. Sites U1403-1405;
351 Norris et al., 2014), and two of the four holes where IW profiles were conducted at Modgunn and
352 Mimir (U1567A, U1569A). At Holes U1568A and U1570A, the two with observed glendonites within
353 the cored strata, the Mg/Ca profiles show an inversion to increasing ratios with depth between around
354 60 – 100 mbsf (Fig. 9C).

355 Results from the PHREEQC modelling for the IW are shown in Fig. 9 and in the supplementary data.
356 Dissolved inorganic carbon (DIC) speciation is shifted towards $[\text{CO}_3^{2-}]$ across the HTV infill and as a
357 result the saturation index of the CaCO_3 minerals increases in these horizons, in the case of calcite to
358 values greater than zero. This indicates that while the measured IW samples reflect a complex
359 diagenetic history, the zones with confirmed glendonite occurrences also have anomalous IW
360 chemistries and carbonate saturation states in present day pore waters.

361 **4. Discussion**

362 *4.1 Ikaite formation and transformation to glendonite*

363 The general microfabric of the glendonites is similar to that observed in previous work on glendonite
364 and transformed ikaite. Notably, areas of calcite blebs (bubble-like mineral inclusions) with Type 1A
365 cores with 2A overgrowths are also observed in glendonites from Cretaceous to Recent in age, and in
366 modern transformed ikaites (Huggett et al., 2005; Grasby et al., 2016; Vickers et al., 2018; Mikhailova
367 et al., 2021; Scheller et al., 2021; Schultz et al., 2023). The presence of a hardened carbonate rim is
368 also a common feature of glendonites (Fig. 4) (Grasby et al., 2017; Scheller et al., 2022; Schultz et al.,

369 2023a; Counts et al., 2023). However, the green Type 0 calcite identified in this study has not been
370 observed in other glendonite thin sections, and appears to be both visually and chemically distinct
371 from the other calcite phases measured in the Exp. 396 glendonites (Fig. 6).

372 Based on the geochemical data, we suggest the following model for the sequential formation of the
373 various calcite phases, as illustrated in Fig. 10:

374 Stage 1: The ikaite grew in the sediments, at or just below the sediment-water interface. The Type 0
375 phase appears to have grown directly onto/against the surface of an ikaite crystal, prior to its
376 decomposition, suggesting it may represent the earliest preserved phase present (Fig. 10).

377 Stage 2: Chemical and thermal conditions changed as burial continued, and the ikaite started to break
378 down (Fig. 10). The formation of 1A blebs began during the recrystallisation reaction, preferentially
379 excluding Mg from the crystal structure, leading to a highly localised increase of Mg^{2+} in the pore
380 waters. This may have taken place over timescales of years (Schultz et al., 2023b). Where breakdown
381 was rapid, larger areas of Type 1B formed (also observed in ikaite transformed on timescales of hours;
382 Schultz et al., 2023b). The faster mineralisation rate of 1A compared to 1B is believed to have caused
383 less discrimination against Mg in the crystal structure, as evidenced by the higher Mg content of 1B
384 compared to 1A (Fig.6). Then, Types 2A and 2B grew, incorporating more Mg into the calcite structure
385 than the Types 1 due to its now higher concentration in the local waters.

386 Stage 3: An undetermined length of time later, after continued burial, Type 3 fibrous syntaxial and/or
387 isopachous sparry calcite forms in some of the pore spaces in the ikaite, growing from the surface of
388 Types 1 and/or 2 calcite phases (Fig. 10). Note that all phases grouped as Types 1 and 2 are believed
389 to have formed directly from ikaite (i.e. the $CaCO_3$ is believed to have been entirely or dominantly
390 sourced directly from the ikaite), whereas we propose that the Type 3 calcite formed from a later
391 diagenetic fluid (e.g. Vickers et al., 2020; Counts et al., 2023). This is based on microfabric and
392 geochemical (elemental and isotopic) data that suggests a very different source fluid. There is very
393 little Type 3 calcite in the Exp. 396 glendonites; much less than is observed in those of the Fur
394 Formation (Vickers et al., 2020). The variable proportion of Type 3 calcite in glendonite is likely
395 responsible for the observed higher bulk Mg/Ca, Mn/Ca and P/Ca ratios than in transformed modern
396 ikaite (Fig. 7).

397 *4.2 Relationship to North Atlantic volcanism and timing of ikaite formation*

398 The glendonites of the Exp. 396 cores are found in latest Paleocene, PETM, and (post-PETM) early
399 Eocene-age sediments, within or just above the intervals containing the most numerous and thickest

400 ash layers (Fig. 2 and 11). The only other reported glendonites from this time interval (Paleocene and
401 early Eocene) are also found in the Nordic Seas region, close to the eruptive sites of the North Atlantic
402 Igneous Province (NAIP). Glendonites have been identified in both Paleocene and Eocene strata in
403 Svalbard (Spielhagen and Tripathi, 2009; Cui et al., 2021), and in early Eocene strata in northern
404 Denmark (Huggett et al., 2005; Vickers et al., 2020; Fig. 1). In the Danish Paleogene successions,
405 glendonites are only found within the early Eocene Fur Formation that contains over 140 macroscopic
406 ash layers of dominantly tholeiitic basalt composition (Fig. 11; Stokke et al., 2020b; Vickers et al.,
407 2020). The Fur Formation corresponds to the ash-rich Balder and Tare formations offshore in the
408 North Sea and Norwegian margin, respectively (King, 2016). The close stratigraphic association with
409 ash layers within the Nordic Basins suggests that ash deposition and/or diagenesis may play a critical
410 role in ikaite precipitation, in contrast to ikaites found in most modern settings. The breakdown of
411 sedimentary C_{org} via sulphate reduction, and/or the anaerobic oxidation of methane (AOM) are
412 thought to play a key role in ikaite precipitation, largely because the low $\delta^{13}C$ values measured in
413 ikaites and glendonites suggest an organic or methanogenic source of carbon (e.g. Rogov et al., 2023
414 and references therein), and also because these organic matter decomposition processes generate
415 DIC (Hiruta and Matsumoto, 2022; Whiticar et al. 2022). Methane has been linked to ikaite/glendonite
416 formation due to their frequent proximity to methane seeps (Greinert and Derkachev, 2004; Teichert
417 and Luppold, 2013; Hiruta and Matsumoto, 2022) and gas inclusions containing methane and other
418 hydrocarbons in glendonite specimens from the Jurassic of Siberia (Morales et al., 2017). However,
419 other studies which examined sedimentary biomarker evidence for AOM in Oligocene and Eocene-
420 aged glendonite-bearing strata did not find evidence for significantly elevated rates of AOM and
421 support an organic matter source for the examined glendonites (Qu et al., 2017; Vickers et al., 2020).

422 For ikaite to be precipitated over the more stable $CaCO_3$ polymorphs, factors inhibiting calcite and
423 promoting ikaite precipitation are also required. These may include high alkalinity, high
424 concentrations of phosphate and/or Mg^{2+} , and low temperatures (Rickaby et al., 2006; Zhou et al.,
425 2015; Purgstaller et al., 2017; Stockmann et al., 2018). The NAIP may have played a key role in
426 generating just such conditions for $CaCO_3$ precipitation and the precipitated polymorph being ikaite.
427 Hydrothermal venting of methane and other gases occurred at sites proximal to the NAIP (Svensen et
428 al., 2004; Frieling et al., 2016; Jones et al., 2019; Berndt et al., 2023); and the explosive nature of the
429 NAIP eruptive volcanism could have driven short-term climate cooling ('volcanic winters', e.g. Robock
430 et al., 2000; Schmidt et al., 2016; Stokke et al., 2020a). Furthermore, the large amounts of volcanic
431 ash in the sediments likely underwent rapid diagenesis, generating the chemical conditions in the pore
432 waters that could have inhibited calcite precipitation and therefore promoted ikaite precipitation (e.g.
433 Gislason and Oelkers, 2011; Olsson et al., 2014; Murray et al., 2018). Indeed, ikaite and other

434 carbonates were discovered as travertine in the Hvanná river in the vicinity of the Eyjafjallajökull
435 volcano shortly after eruptive activity began in Spring of 2010 (Olsson et al., 2014).

436 Compositional data from Exp. 396 shows that the ashes, like those from the Fur positive series (Stokke
437 et al., 2020b), are tholeiitic (Fig. 8). Basaltic volcanic material undergoes rapid chemical weathering
438 (e.g. Gislason and Oelkers, 2011), thus we suggest that the chemical alteration of these tholeiitic ashes
439 could have generated the chemical conditions which promoted ikaite formation, which may include
440 increasing alkalinity and $[Ca^{2+}]$, driving changes in aqueous Mg/Ca (e.g. Gislason and Oelkers, 2011;
441 Olsson et al., 2014; Purgstaller et al., 2017; Murray et al., 2018; Tollefsen et al., 2020). The interstitial
442 water measurements from the cores reflect the conditions in the core interstitial waters today, some
443 c. 55 million years since deposition, and therefore do not reflect conditions immediately prior to ikaite
444 precipitation. Nonetheless, these pore water profiles may provide remnant signatures of post-
445 depositional processes and therefore shed light on how ash diagenesis may have altered local pore
446 water chemistry, promoting ikaite precipitation.

447 The pore water profiles show a strong, sharp change in pH and carbon speciation across the ash-
448 bearing intervals (Fig. 11; Planke et al., 2023b,c), likely a retained signal of the dissolution/leaching of
449 the ashes themselves. While pore water chemistry certainly continued to evolve over the last 55
450 million years, the signature of ash diagenesis on early Paleogene pore waters may have been
451 effectively retained, being buffered against later fluid flow and associated later overprinting reactions
452 by the over- and under-lying clay-rich strata (Planke et al., 2023b,c; Fig. 2). High smectite contents
453 formed from the weathering of silicate material such as basaltic ash both *in situ* and in terrestrial
454 catchment areas, can result in 'aquitard' deposits characterised by very low permeability and low
455 effective porosity (Hendry et al., 2015). This allows large concentration gradients to develop within
456 the sediment pile, as documented along ash-rich margins globally (Torres et al. 1995 and references
457 therein). The major fluctuations in pH, alkalinity, and Mg/Ca ratios across these ash-rich intervals at
458 Modgunn and Mimir (Planke et al., 2023b,c) suggests that these pore waters are likely to have evolved
459 in semi-isolation from over- and underlying strata. Therefore, if the pore water system is closed, the
460 evolution of the pore water chemistry may be limited. Alternatively, long-term diagenesis of ash
461 minerals may be continually altering pore water chemistry across these intervals with some diffusive
462 exchange across the low-permeability clay boundaries, yet still providing an indication of the degree
463 to which ash alteration may impact fluid composition. Pore water measurements through selected
464 cores show that the glendonite-bearing levels associated with volcanic ash are coincident with
465 relatively elevated pH and lower alkalinity, although alkalinity change across ash-rich intervals is less
466 abrupt (Fig. 11). The carbonate chemistry of these pore waters is controlled by a complex balance

467 between CaCO_3 dissolution/precipitation, respiration of organic carbon, and at these sites, probably
468 by alkalinity generation from the dissolution of ash (Longman et al. 2021). As such, it is difficult to
469 ascribe the observed pore water carbonate chemistry changes (Fig. 11) to any one process. However,
470 the relatively high pH and low alkalinity relative to the over- and underlying mud-rich sediments is
471 consistent with alkalinity generation via ash dissolution, resulting in increased TAlk and pH, being
472 counteracted by CaCO_3 precipitation, drawing down carbonate alkalinity. Our observation of abundant
473 CaCO_3 in the form of ikaite and later diagenetic phases in these ash-rich sediments is consistent with
474 this hypothesis. Further, PHREEQC simulations indicate a clear difference in carbonate speciation
475 across ash-rich, glendonite bearing intervals with lower $[\text{CO}_2]_{\text{aq}}$, and higher $[\text{CO}_3^{2-}]$ and $[\text{CaCO}_3^0]$ (Fig.
476 9) compared with surrounding intervals. Aragonite and calcite saturation indices go from under- to
477 oversaturated, and dolomite shows enhanced oversaturation, across these intervals (Fig. 9). Overall,
478 while this indicates that the conditions necessary for ikaite formation prevailed in the hydrothermal
479 vent infill (Fig. 9), we note that the carbonate chemistry of the remnant pore water profiles is
480 characterised by conditions that are far less saturated with respect to CaCO_3 minerals than those
481 necessary to form ikaite in the laboratory, especially at higher temperatures (Purgstaller et al., 2017;
482 Tollefsen et al., 2020).

483 *4.3 Timing and conceptual model for ikaite growth*

484 Zhou et al. (2015) examined modern marine sedimentary ikaite bearing sites and identified “Ikaite
485 Formation Zones” (IFZs) based on where the decreasing $[\text{Ca}^{2+}]$ downcore profile intersects the
486 increasing DIC profile (calculated by maximum $[\text{Ca}^{2+}] \times \text{DIC}$). The IFZ is thus highly variable, as it
487 depends on the amount of organic matter (carbon source) present, which in turn is linked to processes
488 such as sedimentation rate and primary productivity. In modern settings, this is generally between 2
489 – 15 m within the sediment pile (Zhou et al., 2015). In the early Paleogene Norwegian Margin, infill
490 sedimentation rates of hydrothermal vent complex craters were very high. Taking the very
491 conservative estimate of a hydrothermal vent infill duration of 43 kyr for the Modgunn crater (Berndt
492 et al., 2023), the glendonite-bearing horizons for the vent infill cores would have been at depths of
493 below 15 m within 8 kyr for Hole U1568A and 16.5 kyr for Hole U1567C. For sediments such as those
494 encountered in Modgunn and Mimir, the primary driver of DIC was likely AOM, since there was
495 significant methane venting around the NAIP at the time (Svensen et al., 2004; Frieling et al., 2016);
496 and TOC in the sediments is relatively low (generally $< 1.5 \text{ wt } \%$; Planke et al., 2023b,c), which suggests
497 that bacterial sulphate reduction of organic matter could not have been the main source of carbon
498 .The source of $[\text{Ca}^{2+}]$ is believed to result from diagenesis of the ashes (e.g. Gislason and Oelkers,
499 2011). Given that the diagenesis of fresh volcanic material occurs very rapidly after deposition (on

500 timescales of shorter than a month; Hembury et al., 2012; Olsson et al., 2014), the ikaite formation
501 zones are likely to have been much shallower than 15 m at the time of ikaite precipitation, possibly
502 near the sediment-water interface. Observations on the relationship between the Exp. 396
503 glendonites and the host sediments support this theory of very shallow ikaite formation depths. For
504 example, it can be seen that the pale grey sediment is displaced immediately around the glendonite
505 shown in Fig. 3G, yet an ash layer 2 cm above shows no displacement. In Fig. 3H, the pale grey
506 sediment that the glendonite has grown in is displaced, yet the ash that is deposited on top, two thirds
507 up the height of the glendonite, shows no displacement at the top, suggesting the top of the ikaite
508 crystal was potentially protruding into the water column from the seafloor at the time of the ash fall.
509 Therefore, it can be deduced that these parent ikaites grew in the soft sediment prior to compaction,
510 possibly just centimetres below the sediment-water interface. In the Danish succession, similar
511 “boudinage” textures are observed around both glendonites and tree branch fossils in the Fur
512 Formation (Schultz et al., 2022). This indicates that the ikaites grew at or close to the sediment-water
513 interface, as they exhibit the same relationship to the host sediment as tree branches that came to
514 rest on top of or sticking into the top few centimetres or decimetres of sediment. In case of the Exp.
515 396 glendonites, which occur in rapidly deposited sediments, the parent ikaites must have grown
516 quickly, on timescales of years, for these relationships to be observed. Modern ikaites have been
517 known to grow to cm-scale crystals on timescales of months to years (Boch et al., 2015; Schultz et al.,
518 2022, 2023a), suggesting that this is indeed possible. In one case, one month after final construction
519 of a concrete riverbed in Alpine Austria, cm-thick ikaite crystal aggregates were discovered to have
520 formed (Boch et al., 2015); in another instance, ikaite crystals 3 cm long were found growing next to
521 a reservoir causeway in Utqiagvik, Alaska, some 3 years after its construction (Schultz et al., 2022;
522 2023a).

523 Thus, we argue that the parent ikaites to Exp. 396 glendonites grew on geologically synchronous
524 timescales to the sediments in which they are found. Their occurrence and rapid growth during the
525 Paleocene-Eocene greenhouse climate were likely facilitated by the unique conditions near the active
526 NAIP. We propose a scenario in which the chemical environment that stabilised ikaite was provided
527 by the NAIP hydrothermal vent formation and early and rapid diagenesis of the (frequent) ashes
528 deposited from this LIP. The explosive NAIP volcanism may have also may also have played a critical
529 role in driving short-term (c. sub-decadal scale) cooling which additionally helped promote the
530 formation of ikaite.

531 Paleotemperature estimates for the PETM and early Eocene from both biomarkers and stable and
532 clumped isotope thermometry for the North Atlantic and Nordic Seas region (e.g. (Schoon et al., 2015;

533 Stokke et al., 2020; Vickers et al., 2020; Meckler et al., 2022; Rush et al., 2023) show variable
534 temperatures and intervals of cooling which are apparently at odds with global records (e.g.
535 Westerhold et al., 2020)). This has led to speculation that short, sharp, transient cooling events
536 occurred, possibly only on a regional scale (Stokke et al., 2020a; Vickers et al., 2020), as evidence for
537 sudden/short duration cooling is absent from some nearby and other northern Hemisphere sites from
538 similar time periods (e.g. Belgian/Paris basin, Evans et al., 2018; West Siberian Sea and the Arctic,
539 Frieling et al., 2014 and references therein), all of which were characterised by SST of ~20-30°C during
540 this time. Alternatively, however, these discrepancies may reflect changes in sourcing, production
541 depth or seasonal biases in the specific proxies used (e.g. Jia et al., 2017; Udoh et al., 2022; de Winter
542 et al., 2021), or, in the case of carbonate clumped isotopes, solid-state reordering pushing the
543 apparent temperature up (Henkes et al., 2014), or kinetic disequilibrium during the carbonate
544 precipitation (Daëron et al., 2019), meaning that these signals may be challenging to interpret as
545 reflecting true aquatic temperatures at the time of formation in some settings.

546 Regional-scale cooling episodes may result from, for example, a series of short-lived volcanic ‘winters’
547 caused by sulphur degassing during effusive and explosive eruptions (Robock et al., 2000; Schmidt et
548 al., 2016; Stokke et al., 2020a). Given the sub-decadal residence time of sulphur in the atmosphere,
549 this climate forcing would require many closely-spaced eruptions to maintain its cooling effect on
550 timescales of centuries to millennia (Jones et al., 2016). However, since ikaite appears to have grown
551 very rapidly in some of the successions in the Nordic Seas, a growth rate of this magnitude does not
552 seem implausible.

553 In addition to possible volcanically-driven regional climatic events, the unique paleogeography of the
554 region were likely critical for providing the conditions required for ikaite formation. The Nordic Seas
555 were a series of hydrographically and/or geographically semi-restricted, relatively shallow basins with
556 varying connectivity to the Atlantic, Tethys, and Arctic oceans across the Paleocene–Eocene interval
557 (Fig. 1), with several lines of evidence suggesting that maximum restriction occurred in the post-PETM
558 early Eocene (Zacke et al., 2009; Hovikoski et al., 2021; Jones et al., 2023). Such restricted conditions
559 could imply bottom waters in individual basins (simultaneously or at different times) may have been
560 effectively isolated from the global ocean. Without sufficient exchange with the global ocean, bottom
561 waters colder than the global deep ocean, that may have formed during transient cool conditions such
562 as anomalously long and cold (e.g., volcanic-driven) winters, could have led to the formation of a cold
563 bottom layer in a heavily stratified water column in the Nordic Sea basins for a prolonged period.
564 Finally, the thermal uplift and emplacement of a continental flood basalt province created an
565 extensive high-altitude plateau to the west of the shallow seaways that marked the region, which is

566 likely to have altered the positioning, oscillation, and intensity of the Paleogene northern hemisphere
567 jet stream (Jones et al., 2023). While no studies have investigated this potential effect, it is reasonable
568 to assume that a regional microclimate was likely present in the Nordic Seas region at this time. It is
569 possible that a combination of factors led to a bias towards the recording of winter temperatures in
570 the bottom waters of the basin (Vickers et al., 2020). If a long, severe cooling forcing such as a
571 sustained volcanic winter occurred, cooling of the surface waters could eventually have triggered a
572 dense water cascade, bringing these cold, dense waters to the bottom of the basin system. Being
573 restricted and stratified, these cold waters could potentially have remained at the bottom of the basin
574 system for a long time (years) (e.g. Vickers et al., 2020) such that, together with ample volcanic ash
575 supply, it seems plausible that the local conditions coincided to create the necessary conditions for
576 ikaite growth in a hothouse climate.

577 **5. Conclusions**

578 Glendonites are found throughout the Late Paleocene and early Eocene sediments from the IODP Exp.
579 396 cores, including those deposited during the PETM, and closely associated with the volcanic ashes
580 from the nearby NAIP. High-resolution examination and sedimentary logging of these cores reveals
581 ten glendonite horizons, six in the post-PETM sections recovered from the Mimir transect, three from
582 the PETM interval of the hydrothermal vent infill collected in the Modgunn Transect, and one from
583 the pre-PETM interval of this hydrothermal vent infill. Observations of their relationship to their host
584 sediments suggest they grew within centimetres of the sediment-water interface, sometimes even
585 protruding into the water column. Based on known time-scales of ash diagenesis and ikaite growth,
586 we argue that the parent ikaites grew rapidly, within timescales of years to decades after ash
587 deposition. Examination of thin-sections of the glendonites via a number of geochemical methods
588 reveals that the Exp. 396 glendonites show a range of carbonate phases, including fabrics not
589 previously observed in other glendonites nor transformed natural ikaite. These features suggest that
590 their parent ikaite growth environment was unusual even for ikaite, and the leaching and rapid early
591 diagenesis of the NAIP volcanic ashes likely generated the required pore water conditions that
592 stabilised ikaite over other calcium carbonate polymorphs. Paleothermometry studies for the Nordic
593 Seas Region during this time suggest that seawater temperatures were punctuated by remarkably
594 cold, short-term events, although no such temperature deviations have been found outside of this
595 region. Glendonites are also found in the Paleocene and Eocene succession of Svalbard, and in the
596 early Eocene (post-PETM) succession of Denmark, but nowhere outside of this semi-enclosed shallow
597 basin.

598 The close association of glendonites to ash in the Exp. 396 succession, and likewise in the early Eocene
599 of Denmark, along with biomarker and clumped isotope thermometry evidence of episodic transient
600 cooling events, supports our theory that the eruptive phases of the NAIP led to ikaite precipitation in
601 the Nordic Seas region. This was both a chemical and thermal effect: the early diagenesis of the ashes
602 likely drove pore water conditions chemically favourable to ikaite, and the eruptions could have
603 caused transient volcanic winters that were much colder than the prevailing background climate of
604 the time. The unique paleogeography of the region may have led to the basin bottom waters being
605 biased towards these anomalously cold temperatures for years or even decades, allowing the ikaites
606 to grow to the centimetre to >decimetre sizes we observe. Further work is required to test this
607 hypothesis, including detailed, high resolution multi-proxy temperature reconstructions e.g. via
608 clumped isotope thermometry of the glendonites themselves, and biomarker and palynological
609 assemblage-based temperature reconstructions for the sediments of these cores.

610 **Figures and Tables**

611 **Figure 1: (A)** Paleogeographic map of the Nordic Seas region with North Atlantic Igneous Province
612 volcanism shown, after Jones et al. (2023). Location of all known Paleocene – Eocene glendonite
613 bearing sites marked – Exp. 396 Modgunn and Mimir cores (this study); Paleogene-Eocene sediments
614 of Svalbard (Spielhagen and Tripathi, 2009), and early Eocene Fur Formation of northern Denmark
615 (Vickers et al., 2020). **(B)** High-resolution 3-D seismic data for holes 1568 and 1567 along the Modgunn
616 transect (from Planke et al., 2023b). **(C)** High-resolution 3-D seismic data for holes 1569 and 1570
617 along the Mimir Transect (from Planke et al., 2023c). Holes from which glendonites were recovered
618 are shown in red. PETM intervals are shown in yellow.

619 **Figure 2:** Overview logs of the cores with glendonite horizons marked by the red glendonite cartoon.
620 **(A)** The Mimir (U1569 - U1570) transect, from Planke et al. (2023c). The PETM interval (pale yellow)
621 is identified by biostratigraphy (Planke et al., 2023c) and carbon isotope stratigraphy (this study). **(B)**
622 The Modgunn (U1567 - U1568) transect, from Planke et al. (2023b) and Berndt et al., 2023. Core
623 sections of PETM age are highlighted in yellow, and the hydrothermal vent infill (e.g. Fig. 1B) is shown
624 in grey. All correlations between cores are supported by lithologic change, biostratigraphic zonation
625 (Planke et al., 2023b, Berndt et al., 2023), and carbon isotope stratigraphy (Berndt et al., 2023; this
626 study).

627 **Figure 3:** Photographs of glendonites *in situ* in the cores from the Modgunn and Mimir transects. **(A)**
628 Glendonite fragments in drill mud from 1567C-10X-3 40-45 (MLV 86). **(B)** Glendonite from section
629 1567C-11X-1 94-95 (MLV 57, 97). **(C)** Cemented glendonite from section 1569A-19R-2 54-62 (MLV 90).

630 **(D)** Porous carbonate mush interpreted as glendonite from section 1568A-15X-4 (MLV 88). **(E)** Porous
631 cemented glendonite incorporating host sediment from section 1568A-15X-1. **(F)** Glendonite from
632 section 1570A-15R-1 108-112 (MLV 92). **(G)** Glendonite fragment in 1570A-15R-1 22-25 (MLV 91). **(H)**
633 Glendonite from section 1570A-25R-1 (MLV 93). **(I)** Small cemented glendonite fragment from section
634 1570A-22R-2. **(J)** *In situ* fragment of glendonite from section 1570A-24R-1.

635 **Figure 4:** Photomicrographs of polished thin sections from selected Exp. 396 glendonites. The blue
636 background colour is derived from the resin rather than the glendonite. **(A)** and **(B)** show the typical
637 harder outer rim with more porous centre characteristic of transformed ikaite (e.g. Schultz et al.,
638 2023a). Red dots labelled 8, 9 and 10 are spots where LA ICP-MS analysis was performed. The
639 glendonites commonly show areas of different calcite types defined by colour, which are often hard
640 to place into the “traditional” carbonate phase types seen in other glendonites (e.g. Huggett et al.,
641 2005; Vickers et al., 2018). **(C)** shows a distinct boundary between white Type 2B calcite and brown
642 Type 1B calcite, neither of which show zoning defined by colour or porosity. **(D)** shows the sharp
643 boundary between green Type 0 carbonate, with black dendritic surface growth, and other calcite
644 phases. The shape of the sharp boundary that Type 0 defines on one side suggests that Type 0 grew
645 on the surface of and out from an ikaite crystal, which later broke down to leave void space and
646 patches of Type 1B with 2B overgrowths. **(E)** and **(F)** show patches of more typical zoned calcite blebs,
647 here labelled 1A and 2A, which appear to fit into the traditional categories of “Type I” (zoned brown
648 calcite forming the centre of the blebs) and “Type II” (zoned pale overgrowths on Type I; e.g. Vickers
649 et al., 2018; Schultz et al., 2023a). **(G)** Apparent reversal of the “typical” glendonite fabric, whereby
650 the central area of the calcite blebs is pale/white Type 2B and the overgrowth brown Type 1B calcite.
651 This contrasts with **(H)** which shows dark Type 1A with white Type 2A overgrowths.

652 **Figure 5:** Light microscopy, SEM photomicrographs and EDS element maps from thin sections of
653 glendonites at 1569A-19R-2 and 1567C-11X-1. **(A)** Overview under plane polarised light of the area
654 examined for glendonite at 1569A-19R-2, with the carbonate phases labelled. **(B)** BSE image of the
655 same area. Higher porosity in the Type 1 can be seen. **(C)** BSE image of zoomed in area of Type 2B with
656 Type 1B overgrowth. Higher porosity of Type 1 is again clear. **(D)** EDS map showing Mg distribution
657 across calcite types 1B and 2B, overlaid on the BSE photomicrograph. **(E)** The same map without the
658 BSE photomicrograph **(F)** EDS map showing Mg distribution across calcite types 1A, 2A and 2B. **(G)**
659 Overview under plane polarised light of the area examined for glendonite at 1567C-11X-1. **(H)** BSE
660 image of the same area, with pop-out **(I)** showing the microcrystalline nature of Type 0. **(J)**
661 Magnification of the same area with types 1B and 2B calcite under BSE. **(K)** EDS element map showing
662 the Mg distribution across the same area.

663 **Figure 6:** LA ICP-MS element/Ca data for points across the Exp. 396 glendonite polished thin sections.
664 The data have been grouped according to the calcite types described in the main text and in the
665 preceding figures. Photomicrograph showing the location points 8 – 11 from outer edge inwards are
666 shown bottom right, and also in Fig. 4A. Photomicrographs showing the location of all the individual
667 points measured may be found in the Supplementary Material.

668 **Figure 7:** Element/Ca ratios of the Exp. 396 glendonites and associated calcites compared to published
669 ICP-OES data for other glendonite-bearing sites.

670 **Figure 8: (A)** A Total Alkali Silica (TAS) plot comparing the Exp. 396 ashes (this study) to published data
671 for both positive (Stokke et al. 2020b) and negative (Larsen et al., 2003) ash series of the Fur Formation
672 in northern Denmark. The Exp. 396 ashes and Fur positive series fall into the basaltic fields, whereas
673 the Fur negative series show much more variation and have overall more felsic compositions. Note
674 that while the Fur positive series data are microprobe analyses of matrix glass, the Fur Negative series
675 data are whole rock data. However, the whole rock samples were leached of clay prior to analysis and
676 no significant dilution is expected. **(B)** Ternary Alkali-Iron-Magnesium (AFM) diagram showing that the
677 basaltic ashes from both the Exp. 396 sites and the Fur positive series are tholeiitic basalts. Note that
678 many of the Exp. 396 ashes have higher MgO content than the Fur positive ashes.

679 **Figure 9:** (A) PHREEQC simulation results for carbonate speciation in the U1568A core, which spans
680 the hydrothermal vent infill (grey highlight labelled 'HTV'). Note that HCO_3^- (the major species) is not
681 shown. (B) PHREEQC simulation saturation indices for several carbonate polymorphs. (C) IW Mg/Ca
682 profiles for all glendonite-bearing cores (Planke et al., 2023b,c).

683 **Figure 10:** Schematic of ikaite transformation in the Exp. 396 cores, adapted from Counts et al. (2023)
684 based on observed textural relationships and geochemistry of the calcite phases in the Exp. 396
685 glendonites.

686 **Figure 11: (A)** Relative position of glendonites in the Paleocene-Eocene sediments of selected cores
687 from the mid-Norwegian Margin, Exp. 396, compared to measured ash thicknesses. Pore water
688 alkalinity and pH data (Planke et al., 2023b,c) are also shown. Pale grey indicates the PETM-aged
689 intervals in the stratigraphy. Note that for U1569A, core recovery was poor, particularly in the bottom,
690 ash-bearing part (see Fig. 2). High ash contents lead to lower core recovery as they are coarse-grained
691 and unlithified; therefore it is likely that there were much more numerous and thicker ash horizons in
692 the interval between 18R and 37R (c. 180 – 340 mbsf). **(B)** Relative position of glendonites in the
693 Paleocene-Eocene sediments of Northern Denmark, compared to ash thicknesses per metre (Jones et

694 al., 2023). Glendonite horizons for the Fur Formation are from Vickers et al., (2020) (solid lines) and
695 dashed line as identified by Henrik Friis, pers. comm. Pale grey indicates the end of the body of the
696 PETM carbon isotope excursion (Jones et al., 2023). The recovery phase is between ashes -33 and -
697 21a. SC = Stolleklint Clay.

698 **Table 1:** Glendonites of the Exp. 396 cores, PXRD data from bulk glendonite analysis, element/Ca
699 ratios.

700 **Table 2:** Descriptions of the different carbonate phases observed within the glendonites through thin
701 section microscopic and geochemical analysis (light microscopy, SEM, EDS and LA-ICP-MS).

702 **Team List**

703 The IODP expedition 396 Scientists are: S. Planke, C. Berndt, C.A. Alvarez Zarikian, A. Agarwal, G.D.M.
704 Andrews, P. Betlem, J. Bhattacharya, H. Brinkhuis, S. Chatterjee, M. Christopoulou, V.J. Clementi, E.C.
705 Ferré, I.Y. Filina, J. Frieling, P. Guo, D.T. Harper, M.T. Jones, S. Lambart, J. Longman, J.M. Millett, G.
706 Mohn, R. Nakaoka, R.P. Scherer, C. Tegner, N. Varela, M. Wang, W. Xu, and S.L. Yager.

707 **Author contribution**

708 MLV designed the study, undertook sampling and high-resolution logging, photographed and
709 examined thin-sections under a light microscope and SEM, co-ran LA-ICPMS analysis, lead the writing
710 of the manuscript.

711 MTJ undertook PHREEQC modelling, assisted in the interpretation of the data and co-wrote the
712 manuscript.

713 JL undertook the ash thickness measurements, assisted in the interpretation of the data, co-wrote the
714 manuscript and assisted with the logging and sampling.

715 DE ran the LA-ICPMS and assisted in the interpretation of the data and writing of the manuscript.

716 CVU undertook the ICP-OES analysis.

717 ES carried out microprobe analysis of the ashes and plotting of this data.

718 MV undertook the PXRD analysis.

719 JF assisted in the interpretation of the data and co-wrote the manuscript.

720 DTH assisted in the interpretation of the data and co-wrote the manuscript.

721 VJC assisted in the interpretation of the pore-water data and co-wrote the manuscript.

722 IODP E396 S: undertook drilling of the cores, all shipboard analysis, and sampling.

723 **Competing interests**

724 The authors declare that they have no conflict of interest.

725 **Acknowledgements**

726 This research used samples and/or data provided by the International Ocean Discovery Program
727 (IODP). IODP is funded by the US National Science Foundation (NSF), Japan's Ministry of Education,
728 Culture, Sports, Science and Technology (MEXT), The European Consortium for Ocean Research
729 Drilling (ECORD), China's Ministry of Science and Technology (MOST), Australian-New Zealand IODP
730 Consortium (ANZIC), and India's Ministry of Earth Science (MoES). We thank the master, crew, and
731 technical support staff of the JOIDES Resolution during IODP Expedition 396. We gratefully
732 acknowledge funding for this study from the European Commission, Horizon 2020 (ICECAP; grant no.
733 101024218 to MLV) and from the Research Council of Norway through the Centres of Excellence
734 funding scheme, project numbers 223272 (CEED), and 332523 (PHAB), and the Goldschmidt
735 Laboratory national infrastructure (project number 295894). JF acknowledges funding from UK IODP
736 grant NE/W007142/1. We personally thank Ray Leadbitter and Independent Petrographic Services Ltd
737 for making the thin sections used in this study, Siri Simonsen for use and running of the SEM at the
738 University of Oslo. VJC was supported by NSF grant OCE-2205921. FIERCE is financially supported by
739 the Wilhelm and Else Heraeus Foundation and by the Deutsche Forschungsgemeinschaft (DFG: INST
740 161/921-1 FUGG, INST 161/923-1 FUGG and INST 161/1073-1 FUGG), which is gratefully
741 acknowledged. This is FIERCE contribution No. 136. We thank Dr. John W. Counts for his input on
742 discussions of ikaite-glendonite transformation. We thank our reviewers, Dr. Mikhail Rogov, Dr. Niels
743 de Winter and one anonymous reviewer for their insightful constructive comments and feedback.

744 **References**

745 Alley, N.F., Hore, S.B. and Frakes, L.A.. Glaciations at high-latitude Southern Australia during the Early
746 Cretaceous. *Aust. J. Earth Sci.*, 67(8), 1045-1095, <https://doi.org/10.1080/08120099.2019.1590457>,
747 2020

748 Berndt, C., Planke, S., Alvestad, E., Tsikalas, F., and Rasmussen, T. Seismic volcanostratigraphy of the
749 Norwegian Margin: constraints on tectonomagmatic break-up processes. *J. Geol. Soc. London*, 158(3),
750 413–426. <https://doi.org/10.1144/jgs.158.3.413>, 2001.

751 Berndt, C., Planke, S., Alvarez Zarikian, C.A., Frieling, J., Jones, M.T., Millett, J.M., Brinkhuis, H., Bünz,
752 S., Svensen, H.S., Longman, J., Scherer, R.P., Karstens, J., Manton, B., Nelissen, M., Reed, B., Faleide,
753 J.I., Huismans, R.S., Agarwal, A., Andrews, G.D.M., Betlem, P., Bhattacharya, J., Chatterjee, S.,
754 Christopoulou, M., Clementi, V.J., Ferré, E.C., Filina, I.Y., Guo, P., Harper, D.T., Lambart, S., Mohn, G.,
755 Nakaoka, R., Tegner, C., Varela, N., Wang, M., Xu, W., Yager, S.L. (2023). Shallow-water hydrothermal
756 venting linked to the Paleocene Eocene Thermal Maximum. *Nat. Geosci.*, 1-7.
757 <https://doi.org/10.1038/s41561-023-01246-8>, 2023.

758 Boch, R., Dietzel, M., Reichl, P., Leis, A., Baldermann, A., Mittermayr, F. and Pölt, P.. Rapid ikaite
759 (CaCO₃· 6H₂O) crystallization in a man-made river bed: hydrogeochemical monitoring of a rarely
760 documented mineral formation. *Appl. Geochem.*, 63, 366-379,
761 <https://doi.org/10.1016/j.apgeochem.2015.10.003>, 2015.

762 Buchardt, B., Israelson, C., Seaman, P. and Stockmann, G. Ikaite tufa towers in Ikka Fjord, southwest
763 Greenland: their formation by mixing of seawater and alkaline spring water. *J. Sediment. Res.*, 71(1),
764 176-189. <https://doi.org/10.1306/042800710176>, 2001.

765 Council, T.C. and Bennett, P.C. Geochemistry of ikaite formation at Mono Lake, California: implications
766 for the origin of tufa mounds. *Geology*, 21(11), 971-974. [https://doi.org/10.1130/0091-
767 7613\(1993\)021<0971:GOIFAM>2.3.CO;2](https://doi.org/10.1130/0091-7613(1993)021<0971:GOIFAM>2.3.CO;2), 1993.

768 Counts, J.W., Vickers, M.L., Stokes, M.R., Spivey, W., Gardner, K.F., Self-Trail, J.M., Gooley, J.T.,
769 McAleer, R.J., Jubb, A.M., Houseknecht, D.W., Lease, R.O., Griffis, N.P., Vickers, M., Śliwińska, K.,
770 Tompkins, H.G.D., Hudson, A. Insights into the formation of glendonite from the upper Oligocene
771 Sagavanirktok Formation, North Slope, Alaska. Geological Society of America Annual Meeting
772 Abstracts with Programs, 55, 6. <https://doi.org/10.1130/abs/2023AM-391186>, 2023

773 Daëron, M., Drysdale, R.N., Peral, M., Huyghe, D., Blamart, D., Coplen, T.B., Lartaud, F. and Zanchetta,
774 G. Most Earth-surface calcites precipitate out of isotopic equilibrium. *Nat. comm.*, 10, 429.
775 <https://doi.org/10.1038/s41467-019-08336-5>, 2019.

776 Dieckmann, G.S., Nehrke, G., Papadimitriou, S., Göttlicher, J., Steininger, R., Kennedy, H., Wolf-
777 Gladrow, D. and Thomas, D.N. Calcium carbonate as ikaite crystals in Antarctic sea ice. *Geophys. Res.*
778 *Let.*, 35(8). <https://doi.org/10.1029/2008GL033540>, 2008.

779 Durrant, S.F. Feasibility of improvement in analytical performance in laser ablation inductively coupled
780 plasma-mass spectrometry (LA-ICP-MS) by addition of nitrogen to the argon plasma. *Fresenius. J. Anal.*
781 *Chem.* 349, 768–771. <https://doi.org/10.1007/BF00325655>, 1994.

782 Evans, D., Müller, W. Automated Extraction of a Five-Year LA-ICP-MS Trace Element Data Set of Ten
783 Common Glass and Carbonate Reference Materials: Long-Term Data Quality, Optimisation and Laser
784 Cell Homogeneity. *Geostand. Geoanal. Res.* 42, 159–188. <https://doi.org/10.1111/ggr.12204>, 2018.

785 Evans, D., Sagoo, N., Renema, W., Cotton, L.J., Müller, W., Todd, J.A., Saraswati, P.K., Stassen, P.,
786 Ziegler, M., Pearson, P.N. and Valdes, P.J. Eocene greenhouse climate revealed by coupled clumped
787 isotope-Mg/Ca thermometry. *P. Natl. Acad. Sci. USA*, 115(6), 1174-1179.
788 <https://doi.org/10.1073/pnas.1714744115>, 2018.

789 Frank, T.D., Thomas, S.G. and Fielding, C.R. On using carbon and oxygen isotope data from glendonites
790 as paleoenvironmental proxies: a case study from the Permian system of eastern Australia. *J.*
791 *Sediment. Res.*, 78(11), 713-723. <https://doi.org/10.2110/jsr.2008.081>, 2008.

792 Frieling, J., Iakovleva, A.I., Reichart, G.J., Aleksandrova, G.N., Gnibidenko, Z.N., Schouten, S. and Sluijs,
793 A. Paleocene–Eocene warming and biotic response in the epicontinental West Siberian Sea. *Geology*,
794 42(9), 767-770. <https://doi.org/10.1130/G35724.1>, 2014.

795 Frieling, J., Svensen, H.H., Planke, S., Cramwinckel, M.J., Selnes, H. and Sluijs, A. Thermogenic methane
796 release as a cause for the long duration of the PETM. *Proceedings of the National Academy of Sciences*,
797 113(43), 12059-12064. <https://doi.org/10.1073/pnas.1603348113>, 2016.

798 Garbe-Schönberg, D., Müller, S., 2014. Nano-particulate pressed powder tablets for LA-ICP-MS. *J. Anal.*
799 *At. Spectrom.* 29, 990–1000. <https://doi.org/10.1039/C4JA00007B>, 2014.

800 Gates-Rector, S. and Blanton, T. The powder diffraction file: a quality materials characterization
801 database. *Powder Diffr.*, 34(4), 352-360. <https://doi.org/10.1017/S0885715619000812>, 2019.

802 Gislason, S.R. and Oelkers, E.H., Chapter 5: Silicate rock weathering and the global carbon cycle.
803 *Frontiers in Geochemistry: Contribution of Geochemistry to the Study of the Earth*, Harmon, R.S. and
804 Parker, A (eds.), Blackwell Publishing Ltd. 84-103. <https://doi.org/10.1002/9781444329957.ch5>, 2011.

805 Greinert, J. and Derkachev, A. Glendonites and methane-derived Mg-calcites in the Sea of Okhotsk,
806 Eastern Siberia: implications of a venting-related ikaite/glendonite formation. *Marine Geology*, 204(1-
807 2), 129-144. [https://doi.org/10.1016/S0025-3227\(03\)00354-2](https://doi.org/10.1016/S0025-3227(03)00354-2), 2004.

808 Grasby, S.E., McCune, G.E., Beauchamp, B. and Galloway, J.M., 2017. Lower Cretaceous cold snaps led
809 to widespread glendonite occurrences in the Sverdrup Basin, Canadian High Arctic. *Geol. Soc. Am.*
810 *Bull.*, 129(7-8), 771-787. <https://doi.org/10.1130/B31600.1>, 2017.

811 Heinrich, C.A., Pettke, T., Halter, W.E., Aigner-Torres, M., Audétat, A., Günther, D., Hattendorf, B.,
812 Bleiner, D., Guillong, M., Horn, I. Quantitative multi-element analysis of minerals, fluid and melt
813 inclusions by laser-ablation inductively-coupled-plasma mass-spectrometry. *Geochim. Cosmochim.*
814 *Ac.* 67, 3473–3497. [https://doi.org/10.1016/S0016-7037\(03\)00084-X](https://doi.org/10.1016/S0016-7037(03)00084-X), 2003.

815 Hembury, D.J., Palmer, M.R., Fones, G.R., Mills, R.A., Marsh, R. and Jones, M.T. Uptake of dissolved
816 oxygen during marine diagenesis of fresh volcanic material. *Geochim. Cosmochim. Ac.*, 84, pp.353-
817 368. <https://doi.org/10.1016/j.gca.2012.01.017>, 2012.

818 Hendry, M. J., Solomon, D. K., Person, M., Wassenaar, L. I., Gardner, W. P., Clark, I. D., Mayer, K. U.,
819 Kunimaru, T., Nakata, K., Hasegawa, T. Can argillaceous formations isolate nuclear waste? Insights
820 from isotopic, noble gas, and geochemical profiles, *Geofluids*, 15, 381–386,
821 <https://doi.org/10.1111/GFL.12132>, 2015.

822 Henkes, G.A., Passey, B.H., Grossman, E.L., Shenton, B.J., Pérez-Huerta, A. and Yancey, T.E.
823 Temperature limits for preservation of primary calcite clumped isotope paleotemperatures. *Geochim.*
824 *Cosmochim. Ac.*, 139, 362-382. <https://doi.org/10.1016/j.gca.2014.04.040>, 2014.

825 Hiruta, A. and Matsumoto, R. Geochemical comparison of ikaite and methane-derived authigenic
826 carbonates recovered from Echigo Bank in the Sea of Japan. *Marine Geology*, 443, 106672.
827 <https://doi.org/10.1016/j.margeo.2021.106672>, 2022.

828 Hovikoski, J., Fyhn, M.B.W., Nøhr-Hansen, H., Hopper, J.R., Andrews, S., Barham, M., Nielsen, L.H.,
829 Bjerager, M., Bojesen-Koefoed, J., Lode, S., Sheldon, E., Uchman, A., Skorstengaard, P.R., Alsen, P.
830 Paleocene-Eocene volcanic segmentation of the Norwegian-Greenland seaway reorganized high-
831 latitude ocean circulation. *Communications Earth & Environment*, 2, 172.
832 <https://doi.org/10.1038/s43247-021-00249-w>, 2021.

833 Huggett, J.M., Schultz, B.P., Shearman, D.J. and Smith, A.J. The petrology of ikaite pseudomorphs and
834 their diagenesis. *P. Geologist. Assoc.*, 116(3-4), 207-220. [https://doi.org/10.1016/S0016-](https://doi.org/10.1016/S0016-7878(05)80042-2)
835 [7878\(05\)80042-2](https://doi.org/10.1016/S0016-7878(05)80042-2), 2005.

836 Jochum, K.P., Garbe-Schönberg, D., Veter, M., Stoll, B., Weis, U., Weber, M., Lugli, F., Jentzen, A.,
837 Schiebel, R., Wassenburg, J.A., Jacob, D.E., Haug, G.H., 2019. Nano-Powdered Calcium Carbonate
838 Reference Materials: Significant Progress for Microanalysis? *Geostand. Geoanal. Res.* 43, 595–609.
839 <https://doi.org/10.1111/ggr.12292>, 2019.

840 Jochum, K.P., Weis, U., Stoll, B., Kuzmin, D., Yang, Q., Raczek, I., Jacob, D.E., Stracke, A., Birbaum, K.,
841 Frick, D.A., Günther, D., Enzweiler, J., 2011. Determination of Reference Values for NIST SRM 610–617
842 Glasses Following ISO Guidelines. *Geostand. Geoanal. Res.* 35, 397–429.
843 <https://doi.org/10.1111/j.1751-908X.2011.00120.x>, 2011.

844 Jones, M.T. and Gislason, S.R., 2008. Rapid releases of metal salts and nutrients following the
845 deposition of volcanic ash into aqueous environments. *Geochim. Cosmochim. Ac.*, 72(15), 3661-3680.
846 <https://doi.org/10.1016/j.gca.2008.05.030>, 2008.

847 Jones, M.T., Jerram, D.A., Svensen, H.H., Grove, C. The effects of large igneous provinces on the global
848 carbon and sulphur cycles. *Palaeogeogr. Palaeocl.*, 441, 4-21.
849 <https://doi.org/10.1016/j.palaeo.2015.06.042>, 2016.

850 Jones, M.T., Pearce, C.R., Jeandel, C., Gislason, S.R., Eiriksdottir, E.S., Mavromatis, V. and Oelkers, E.H.,
851 2012. Riverine particulate material dissolution as a significant flux of strontium to the oceans. *Earth*
852 *Planet. Sc. Lett.*, 355, 51-59. <https://doi.org/10.1016/j.epsl.2012.08.040>, 2012.

853 Jones, M.T., Percival, L.M., Stokke, E.W., Frieling, J., Mather, T.A., Riber, L., Schubert, B.A., Schultz, B.,
854 Tegner, C., Planke, S. and Svensen, H.H. Mercury anomalies across the Palaeocene–Eocene thermal
855 maximum. *Clim. Past*, 15, 217-236. <https://doi.org/10.5194/cp-15-217-2019>, 2019.

856 Jones, M. T., Stokke, E. W., Rooney, A. D., Frieling, J., Pogge von Strandmann, P. A. E., Wilson, D. J.,
857 Svensen, H. H., Planke, S., Adatte, T., Thibault, N., Vickers, M. L., Mather, T. A., Tegner, C., Zuchuat, V.,
858 and Schultz, B. P.: Tracing North Atlantic volcanism and seaway connectivity across the Paleocene–
859 Eocene Thermal Maximum (PETM), *Clim. Past*, 19, 1623–1652, [https://doi.org/10.5194/cp-19-1623-](https://doi.org/10.5194/cp-19-1623-2023)
860 [2023](https://doi.org/10.5194/cp-19-1623-2023), 2023.

861 Kemper, E. (1987). *Das Klima der Kreide-Zeit*. Geologisches Jahrbuch, Hannover, reihe A, 96, 5 – 185.

862 King, C., 2016. A Revised Correlation of Tertiary Rocks in the British Isles and Adjacent Areas of NW
863 Europe. Ed. Gale, A.S. and Barry, T.L. Geol. Soc. London, Special Report No. 27.

864 Larsen, L.M., Fitton, J.G. and Pedersen, A.K., 2003. Paleogene volcanic ash layers in the Danish Basin:
865 compositions and source areas in the North Atlantic Igneous Province. *Lithos*, 71(1), 47-80.
866 <https://doi.org/10.1016/j.lithos.2003.07.001>, 2003.

867 Longman, J., Gernon, T.M., Palmer, M.R., Jones, M.T., Stokke, E.W. and Svensen, H.H. Marine
868 diagenesis of tephra aided the Palaeocene-Eocene Thermal Maximum termination. *Earth Planet. Sc.*
869 *Lett.*, 571, 117101. <https://doi.org/10.1016/j.epsl.2021.117101>, 2021.

870 Meckler, A.N., Sexton, P.F., Piasecki, A.M., Leutert, T.J., Marquardt, J., Ziegler, M., Agterhuis, T.,
871 Lourens, L.J., Rae, J.W.B., Barnet, J., Tripathi, A., and Bernasconi, S.M. Cenozoic evolution of deep ocean
872 temperature from clumped isotope thermometry. *Science*, 377(6601), 86-90.
873 <https://doi.org/10.1126/science.abk0604>, 2022.

874 Merkel, A. and Munnecke, A., 2023. Glendonite-bearing concretions from the upper Pliensbachian
875 (Lower Jurassic) of South Germany: indicators for a massive cooling in the European epicontinental
876 sea. *Facies*, 69(3), 10. <https://doi.org/10.1007/s10347-023-00667-6>, 2023.

877 Mikhailova, K.Y., Rogov, M.A., Ershova, V.B., Vasileva, K.Y., Pokrovsky, B.G. and Baraboshkin, E.Y. New
878 data on stratigraphy and distributions of glendonites from the carolinefjellet formation (Middle
879 Aptian–Lower Albian, Cretaceous), Western Spitsbergen. *Stratigr. Geo. Correl.*, 29, 21-35.
880 <https://doi.org/10.1134/S0869593821010056>, 2021.

881 Morales, C., Rogov, M., Wierzbowski, H., Ershova, V., Suan, G., Adatte, T., Föllmi, K.B., Tegelaar, E.,
882 Reichart, G.J., De Lange, G.J. and Middelburg, J.J. Glendonites track methane seepage in Mesozoic
883 polar seas. *Geology*, 45(6), 503-506. <https://doi.org/10.1130/G38967.1> 2017. Murphy, B.H., Farley,
884 K.A. and Zachos, J.C. An extraterrestrial ³He-based timescale for the Paleocene–Eocene thermal

885 maximum (PETM) from Walvis Ridge, IODP Site 1266. *Geochim. Cosmochim. Ac.*, 74(17), pp.5098-
886 5108. <https://doi.org/10.1016/j.gca.2010.03.039>, 2010.

887 Norris, R.D., Wilson, P.A., Blum, P., Fehr, A., Agnini, C., Bornemann, A., Boulila, S., Bown, P.R.,
888 Cournede, C., Friedrich, O. and Ghosh, A.K. Expedition 342 summary. *Proc. IODP.*
889 [10.2204/iodp.proc.342.101.2014](https://doi.org/10.2204/iodp.proc.342.101.2014), 2014.

890 Olsson, J., Stipp, S.L.S., Dalby, K.N. and Gislason, S.R. Rapid release of metal salts and nutrients from
891 the 2011 Grímsvötn, Iceland volcanic ash. *Geochim. Cosmochim. Ac.*, 123, 134-149.
892 <https://doi.org/10.1016/j.gca.2013.09.009>, 2013.

893 Olsson, J., Stipp, S.L.S., Makovicky, E. and Gislason, S.R. Metal scavenging by calcium carbonate at the
894 Eyjafjallajökull volcano: A carbon capture and storage analogue. *Chem. Geol.*, 384, 135-148.
895 <https://doi.org/10.1016/j.chemgeo.2014.06.025>, 2014.

896 Parkhurst, D.L., and Appelo, C.A.J. Description of input and examples for PHREEQC version 3—A
897 computer program for speciation, batch-reaction, one-dimensional transport, and inverse
898 geochemical calculations: U.S. Geological Survey Techniques and Methods, book 6, chap. A43, 497,
899 <https://doi.org/10.3133/tm6A43>, 2013.

900 Pearce, N.J.G., Perkins, W.T., Westgate, J.A., Gorton, M.P., Jackson, S.E., Neal, C.R., Chenery, S.P. A
901 Compilation of New and Published Major and Trace Element Data for NIST SRM 610 and NIST SRM 612
902 Glass Reference Materials. *Geostandard. Newslett.* 21, 115–144. [https://doi.org/10.1111/j.1751-
903 908X.1997.tb00538.x](https://doi.org/10.1111/j.1751-908X.1997.tb00538.x), 1997.

904 Planke, S., Berndt, C. and Alvarez Zarikian, C.A. and the Expedition 396 scientists. Expedition 396
905 Summary, in Planke, S., Berndt, C., Alvarez Zarikian, C.A., and the Expedition 396 Scientists, Mid-
906 Norwegian Margin Magmatism and Paleoclimate Implications. *Proceedings of the International Ocean
907 Discovery Program*, 396. <https://doi.org/10.14379/iodp.proc.396.101.2023>, 2023a.

908 Planke, S., Berndt, C. and Alvarez Zarikian, C.A. and the Expedition 396 scientists. Sites U1567 and
909 U1568, in Planke, S., Berndt, C., Alvarez Zarikian, C.A., and the Expedition 396 Scientists, Mid-
910 Norwegian Margin Magmatism and Paleoclimate Implications. *Proceedings of the International Ocean
911 Discovery Program*, 396. <https://doi.org/10.14379/iodp.proc.396.105.2023>, 2023b.

912 Planke, S., Berndt, C. and Alvarez Zarikian, C.A. and the Expedition 396 scientists. Sites U1569 and
913 U1570, in Planke, S., Berndt, C., Alvarez Zarikian, C.A., and the Expedition 396 Scientists, Mid-

914 Norwegian Margin Magmatism and Paleoclimate Implications. Proceedings of the International Ocean
915 Discovery Program, 396. <https://doi.org/10.14379/iodp.proc.396.106.2023>, 2023c.

916 Planke, S., Berndt, C. and Alvarez Zarikian, C.A. and the Expedition 396 scientists. Expedition 396
917 Methods, in Planke, S., Berndt, C., Alvarez Zarikian, C.A., and the Expedition 396 Scientists, Mid-
918 Norwegian Margin Magmatism and Paleoclimate Implications. Proceedings of the International Ocean
919 Discovery Program, 396. <https://doi.org/10.14379/iodp.proc.396.102.2023>, 2023d. Purgstaller, B.,
920 Dietzel, M., Baldermann, A. and Mavromatis, V. Control of temperature and aqueous Mg²⁺/Ca²⁺ ratio
921 on the (trans-) formation of ikaite. *Geochim. Cosmochim. Ac.*, 217, 128-143.
922 <https://doi.org/10.1016/j.gca.2017.08.016>, 2017.

923 Qu, Y., Teichert, B.M.A., Birgel, D., Goedert, J.L. and Peckmann, J. The prominent role of bacterial
924 sulfate reduction in the formation of glendonite: a case study from Paleogene marine strata of western
925 Washington State. *Facies*, 63, 1-16. <https://doi.org/10.1007/s10347-017-0492-1>, 2017. Rickaby, R.,
926 Shaw, S., Bennitt, G., Kennedy, H., Zabel, M. and Lennie, A. Potential of ikaite to record the evolution
927 of oceanic $\delta^{18}O$. *Geology*, 34(6), 497-500. <https://doi.org/10.1130/G22413.1>, 2006.

928 Robock, A. Volcanic eruptions and climate. *Rev. Geophys.*, 38(2), 191-219.
929 <https://doi.org/10.1029/1998RG000054>, 2000.

930 Rogov, M.A., Ershova, V.B., Shchepetova, E.V., Zakharov, V.A., Pokrovsky, B.G., and Khudoley, A.K.
931 Earliest Cretaceous (late Berriasian) glendonites from Northeast Siberia revise the timing of initiation
932 of transient Early Cretaceous cooling in the high latitudes: *Cretaceous Res.*, 71, 102–112.
933 <https://doi.org/10.1016/j.cretres.2016.11.011>, 2017.

934 Rogov, M., Ershova, V., Vereshchagin, O., Vasileva, K., Mikhailova, K. and Krylov, A. Database of global
935 glendonite and ikaite records throughout the Phanerozoic. *Earth Syst. Sci. Data*, 13(2), 343-356.
936 <https://doi.org/10.5194/essd-13-343-2021>, 2021.

937 Rogov, M., Ershova, V., Gaina, C., Vereshchagin, O., Vasileva, K., Mikhailova, K. and Krylov, A.
938 Glendonites throughout the Phanerozoic. *Earth-Sci. Rev.*, 104430.
939 <https://doi.org/10.1016/j.earscirev.2023.104430>, 2023.

940 Röhl, U., Westerhold, T., Bralower, T.J. and Zachos, J.C. On the duration of the Paleocene-Eocene
941 thermal maximum (PETM). *Geochemistry, Geophysics, Geosystems*, 8(12).
942 <https://doi.org/10.1029/2007GC001784>, 2007.

943 Rush, W., Self-Trail, J., Zhang, Y., Sluijs, A., Brinkhuis, H., Zachos, J., Ogg, J.G. and Robinson, M.
944 Assessing environmental change associated with early Eocene hyperthermals in the Atlantic Coastal
945 Plain, USA. *Clim. Past*, 19, 1677-1698. <https://doi.org/10.5194/cp-19-1677-2023>, 2023.

946 Scheller, E.L., Grotzinger, J. and Ingalls, M. Guttulatic calcite: A carbonate microtexture that reveals
947 frigid formation conditions. *Geology*, 50(1), 48-53. <https://doi.org/10.1130/G49312.1>, 2022.

948 Schmidt, A., Skeffington, R.A., Thordarson, T., Self, S., Forster, P.M., Rap, A., Ridgwell, A., Fowler, D.,
949 Wilson, M., Mann, G.W. and Wignall, P.B. Selective environmental stress from sulphur emitted by
950 continental flood basalt eruptions. *Nat. Geosci.*, 9(1), 77-82. <https://doi.org/10.1038/ngeo2588>, 2016.

951 Schoon, P.L., Heilmann-Clausen, C., Schultz, B.P., Damasté, J.S.S., Schouten, S. Warming and
952 environmental changes in the eastern North Sea Basin during the Palaeocene–Eocene Thermal
953 Maximum as revealed by biomarker lipids. *Org. Geochem.* 78, 79-88.
954 <https://doi.org/10.1016/j.orggeochem.2014.11.003>, 2015.

955 Schultz, B., Thibault, N. and Huggett, J. The minerals ikaite and its pseudomorph glendonite: Historical
956 perspective and legacies of Douglas Shearman and Alec K. Smith. *P. Geologist. Assoc.*, 133(2), 176-192.
957 <https://doi.org/10.1016/j.pgeola.2022.02.003>, 2022.

958 Schultz, B.P., Huggett, J.M., Kennedy, G.L., Burger, P., Friis, H., Jensen, A.M., Kanstrup, M., Bernasconi,
959 S.M., Thibault, N., Ullmann, C.V., and Vickers, M.L. Petrography and geochemical analysis of Arctic
960 ikaite pseudomorphs from Utqiagvik (Barrow), Alaska, *Norw. J. Geol.*, 103, 202303.
961 <https://dx.doi.org/10.17850/njg103-1-3>, 2023a.

962 Schultz, B.P., Huggett, J., Ullmann, C.V., Kassens, H. and Kölling, M. Links between Ikaite Morphology,
963 Recrystallised Ikaite Petrography and Glendonite Pseudomorphs Determined from Polar and Deep-
964 Sea Ikaite. *Minerals*, 13(7), 841. <https://doi.org/10.3390/min13070841>, 2023b
965 Sluijs, A., Frieling, J., Inglis, G.N., Nierop, K.G., Peterse, F., Sangiorgi, F. and Schouten, S. Late Paleocene–early Eocene Arctic
966 Ocean sea surface temperatures: reassessing biomarker paleothermometry at Lomonosov Ridge.
967 *Clim. Past*, 16(6), 2381-2400. <https://doi.org/10.5194/cp-16-2381-2020>, 2020.

968 Spielhagen, R.F. and Tripathi, A. Evidence from Svalbard for near-freezing temperatures and climate
969 oscillations in the Arctic during the Paleocene and Eocene. *Palaeogeogr. Palaeoclimatol.*, 278(1-4), 48-56.
970 <https://doi.org/10.1016/j.palaeo.2009.04.012>, 2009.

971 Stockmann, G.J., Seaman, P., Balic-Zunic, T., Peternell, M., Sturkell, E., Liljebadh, B. and Gyllencreutz,
972 R. Mineral Changes to the Tufa Columns of Ikka Fjord, SW Greenland. *Minerals*, 12(11), 1430.
973 <https://doi.org/10.3390/min12111430>, 2022.

974 Stockmann, G., Tollefsen, E., Skelton, A., Brüchert, V., Balic-Zunic, T., Langhof, J., Skogby, H. and
975 Karlsson, A. Control of a calcite inhibitor (phosphate) and temperature on ikaite precipitation in Ikka
976 Fjord, southwest Greenland. *Appl. Geochem.*, 89, 11-22.
977 <https://doi.org/10.1016/j.apgeochem.2017.11.005>, 2018.

978 Stokke, E.W., Jones, M.T., Tierney, J.E., Svensen, H.H. and Whiteside, J.H. Temperature changes across
979 the Paleocene-Eocene Thermal Maximum—a new high-resolution TEX86 temperature record from the
980 Eastern North Sea Basin. *Earth Planet. Sc. Lett.*, 544, 116388.
981 <https://doi.org/10.1016/j.epsl.2020.116388>, 2020a.

982 Stokke, E.W., Liu, E.J., Jones, M.T. Evidence of explosive hydromagmatic eruptions during the
983 emplacement of the North Atlantic Igneous Province. *Volcanica*, 3 (2), 227-250.
984 <https://doi.org/10.30909/vol.03.02.227250>, 2020b.

985 Suess, E., Balzer, W., Hesse, K.F., Müller, P.J., Ungerer, C.T. and Wefer, G. Calcium carbonate
986 hexahydrate from organic-rich sediments of the Antarctic shelf: precursors of glendonites. *Science*,
987 216(4550), 1128-1131. <https://doi.org/10.1126/science.216.4550.1128>, 1982.

988 Svensen, H., Planke, S., Malthes-Sørensen, A., Jamtveit, B., Myklebust, R., Rasmussen Eidem, T. and
989 Rey, S.S. Release of methane from a volcanic basin as a mechanism for initial Eocene global warming.
990 *Nature*, 429(6991), 542-545. <https://doi.org/10.1038/nature02566>, 2004.

991 Teichert, B.M.A. and Luppold, F.W. Glendonites from an Early Jurassic methane seep—Climate or
992 methane indicators?. *Palaeogeography, Palaeoclimatology, Palaeoecology*, 390, 81-93.
993 <https://doi.org/10.1016/j.palaeo.2013.03.001>, 2013. Tollefsen, E., Balic-Zunic, T., Mörth, C.M.,
994 Brüchert, V., Lee, C.C. and Skelton, A., 2020. Ikaite nucleation at 35 C challenges the use of glendonite
995 as a paleotemperature indicator. *Sci Rep.-UK*, 10(1), 8141. [https://doi.org/10.1038/s41598-020-](https://doi.org/10.1038/s41598-020-64751-5)
996 [64751-5](https://doi.org/10.1038/s41598-020-64751-5), 2020.

997 Torres, M.E., Marsaglia, K.M., Martin, J.B. and Murray, R.W. Sediment diagenesis in western Pacific
998 basins. *Geoph. Monog.*, 88, 241-258., 1995.

999 Ullmann, C.V., Boyle, R., Duarte, L.V., Hesselbo, S.P., Kasemann, S.A., Klein, T., Lenton, T.M., Piazza, V.
1000 and Aberhan, M. Warm afterglow from the Toarcian Oceanic Anoxic Event drives the success of deep-
1001 adapted brachiopods. *Sci Rep.-UK*, 10(1), 6549. <https://doi.org/10.1038/s41598-020-63487-6>, 2020.

1002 Vickers, M., Watkinson, M., Price, G.D. and Jerrett, R., 2018. An improved model for the ikaite-
1003 glendonite transformation: evidence from the Lower Cretaceous of Spitsbergen, Svalbard. *Norw. J.*
1004 *Geol.*, 98(1), 1 – 15 <https://dx.doi.org/10.17850/njg98-1-01>, 2018.

1005 Vickers, M.L., Price, G.D., Jerrett, R.M., Sutton, P., Watkinson, M.P. and FitzPatrick, M., 2019. The
1006 duration and magnitude of Cretaceous cool events: Evidence from the northern high latitudes. *Geol.*
1007 *Soc. Am. Bull.*, 131(11-12), 1979-1994. <https://doi.org/10.1130/B35074.1>, 2019.

1008 Vickers, M.L., Lengger, S.K., Bernasconi, S.M., Thibault, N., Schultz, B.P., Fernandez, A., Ullmann, C.V.,
1009 McCormack, P., Bjerrum, C.J., Rasmussen, J.A. and Hougård, I.W. Cold spells in the Nordic Seas during
1010 the early Eocene Greenhouse. *Nat. Comm.*, 11(1), 4713. [https://doi.org/10.1038/s41467-020-18558-](https://doi.org/10.1038/s41467-020-18558-7)
1011 [7](https://doi.org/10.1038/s41467-020-18558-7), 2020.

1012 Vickers, M.L., Vickers, M., Rickaby, R.E., Wu, H., Bernasconi, S.M., Ullmann, C.V., Bohrmann, G.,
1013 Spielhagen, R.F., Kassens, H., Schultz, B.P. and Alwmark, C. The ikaite to calcite transformation:
1014 Implications for palaeoclimate studies. *Geochim. Cosmochim. Ac.*, 334, 201-216.
1015 <https://doi.org/10.1016/j.gca.2022.08.001>, 2022.

1016 Westerhold, T., Marwan, N., Drury, A.J., Liebrand, D., Agnini, C., Anagnostou, E., Barnet, J.S., Bohaty,
1017 S.M., De Vleeschouwer, D., Florindo, F. and Frederichs, T. An astronomically dated record of Earth's
1018 climate and its predictability over the last 66 million years. *Science*, 369(6509), 1383-1387.
1019 <https://doi.org/10.1126/science.aba6853>, 2020.

1020 Whiticar, M.J., Suess, E., Wefer, G. and Müller, P.J. Calcium carbonate hexahydrate (ikaite): History of
1021 mineral formation as recorded by stable isotopes. *Minerals*, 12(12), 1627.
1022 <https://doi.org/10.3390/min12121627>, 2022.

1023 Zachos, J.C., Dickens, G.R. and Zeebe, R.E. An early Cenozoic perspective on greenhouse warming and
1024 carbon-cycle dynamics. *Nature*, 451(7176), 279-283. <https://doi.org/10.1038/nature06588>, 2008.

1025 Zacke, A., Voigt, S., Joachimski, M.M., Gale, A.S., Ward, D.J., Tütken, T. Surface-water freshening and
1026 high-latitude river discharge in the Eocene North Sea. *J. Geol. Soc. London*, 166, 969-980.
1027 <https://doi.org/10.1144/0016-76492008-068>, 2009.

1028 Zhou, X., Lu, Z., Rickaby, R.E., Domack, E.W., Wellner, J.S. and Kennedy, H.A., 2015. Ikaite abundance
1029 controlled by porewater phosphorus level: Potential links to dust and productivity. *J. Geol.*, 123(3),
1030 269-281. <https://doi.org/10.1086/681918>, 2015.

1031

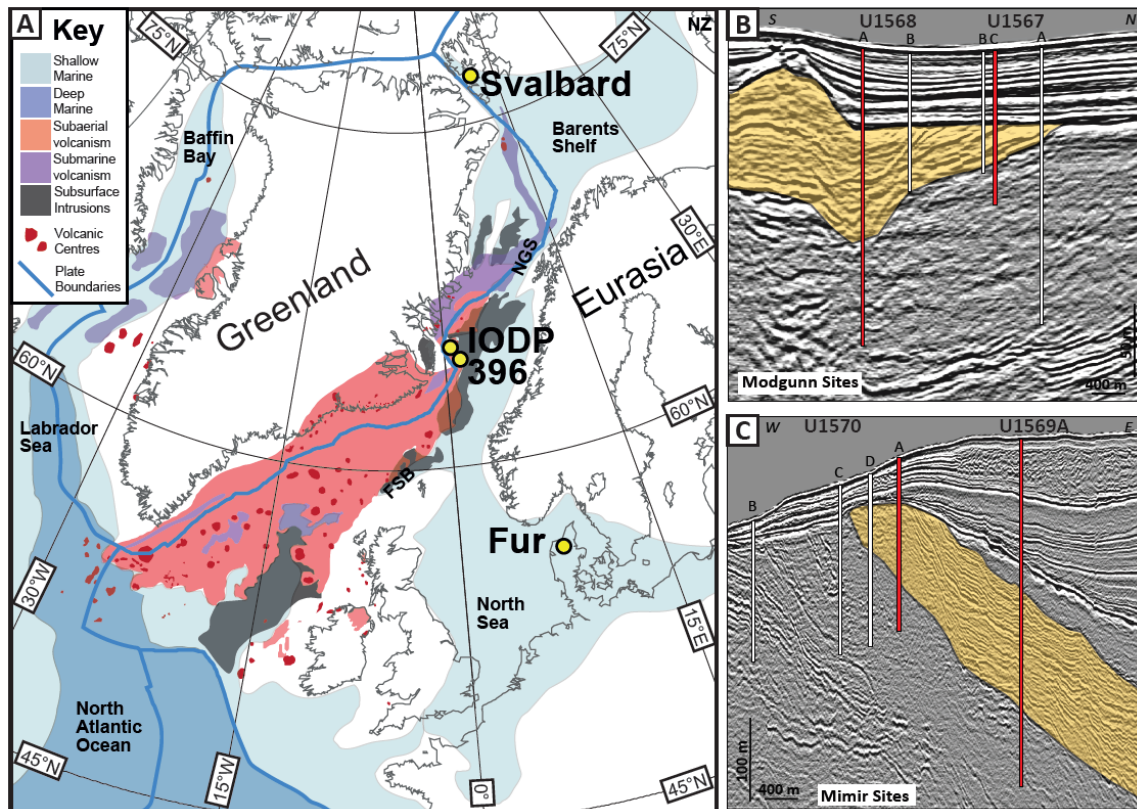


Figure 1: (A) Paleogeographic map of the Nordic Seas region with North Atlantic Igneous Province volcanism shown, after Jones et al. (2023). Location of all known Paleocene – Eocene glendonite bearing sites marked – Exp. 396 Modgunn and Mimir transects (this study); Paleogene-Eocene sediments of Svalbard (Spielhagen and Tripathi, 2009), and early Eocene Fur Formation of northern Denmark (Vickers et al., 2020). (B) High-resolution 3-D seismic data for holes 1568 and 1567 along the Modgunn transect (from Planke et al., 2023). (C) High-resolution 3-D seismic data for holes 1569 and 1570 along the Mimir Transect (from Planke et al., 2023). Holes from which glendonites were recovered are shown in red. PETM intervals are shown in yellow.

1032

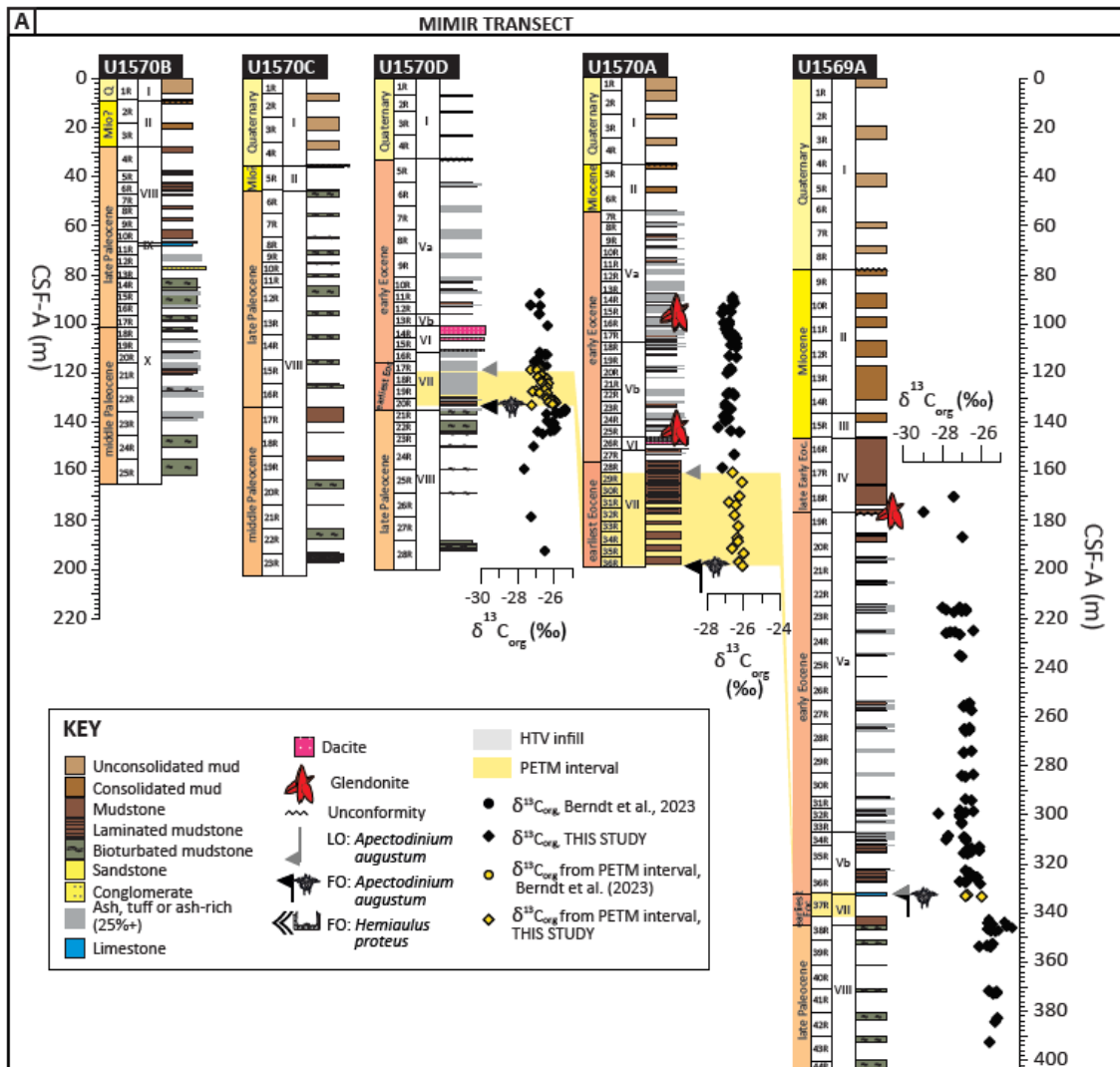
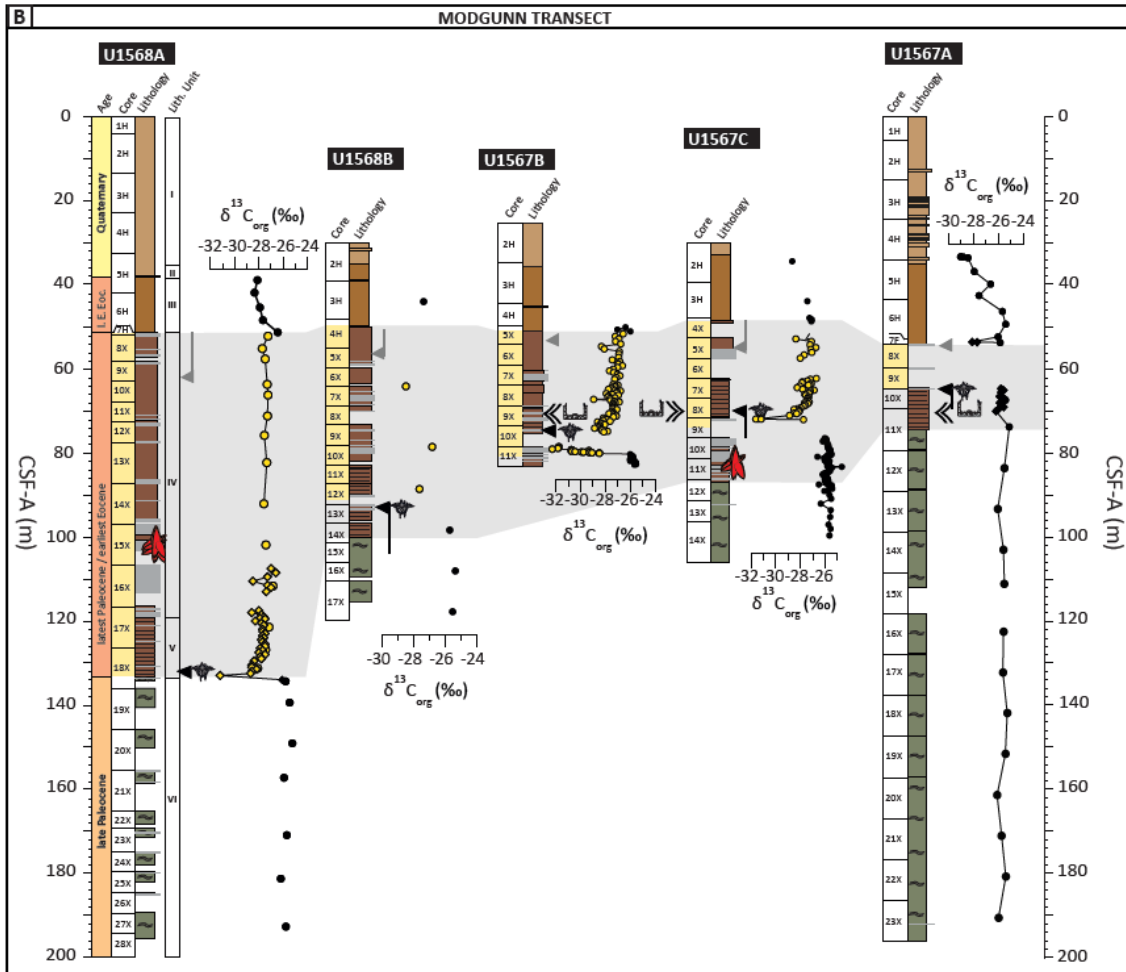


Figure 2: Overview logs of the cores with glendonite horizons marked by the red glendonite cartoon. (A) The Mimir (U1569 - U1570) transect, from Planke et al. (2023c). The PETM interval (pale yellow) is identified by biostratigraphy (Planke et al., 2023c) and carbon isotope stratigraphy (this study). **(B)** The Modgunn (U1567 - U1568) transect, from Planke et al. (2023b) and Berndt et al., 2023. Core sections of PETM age are highlighted in yellow, and the hydrothermal vent infill (e.g. Fig. 1B) is shown in grey. All correlations between cores are supported by lithologic change, biostratigraphic zonation (Planke et al., 2023b, Berndt et al., 2023), and carbon isotope stratigraphy (Berndt et al., 2023; this study).



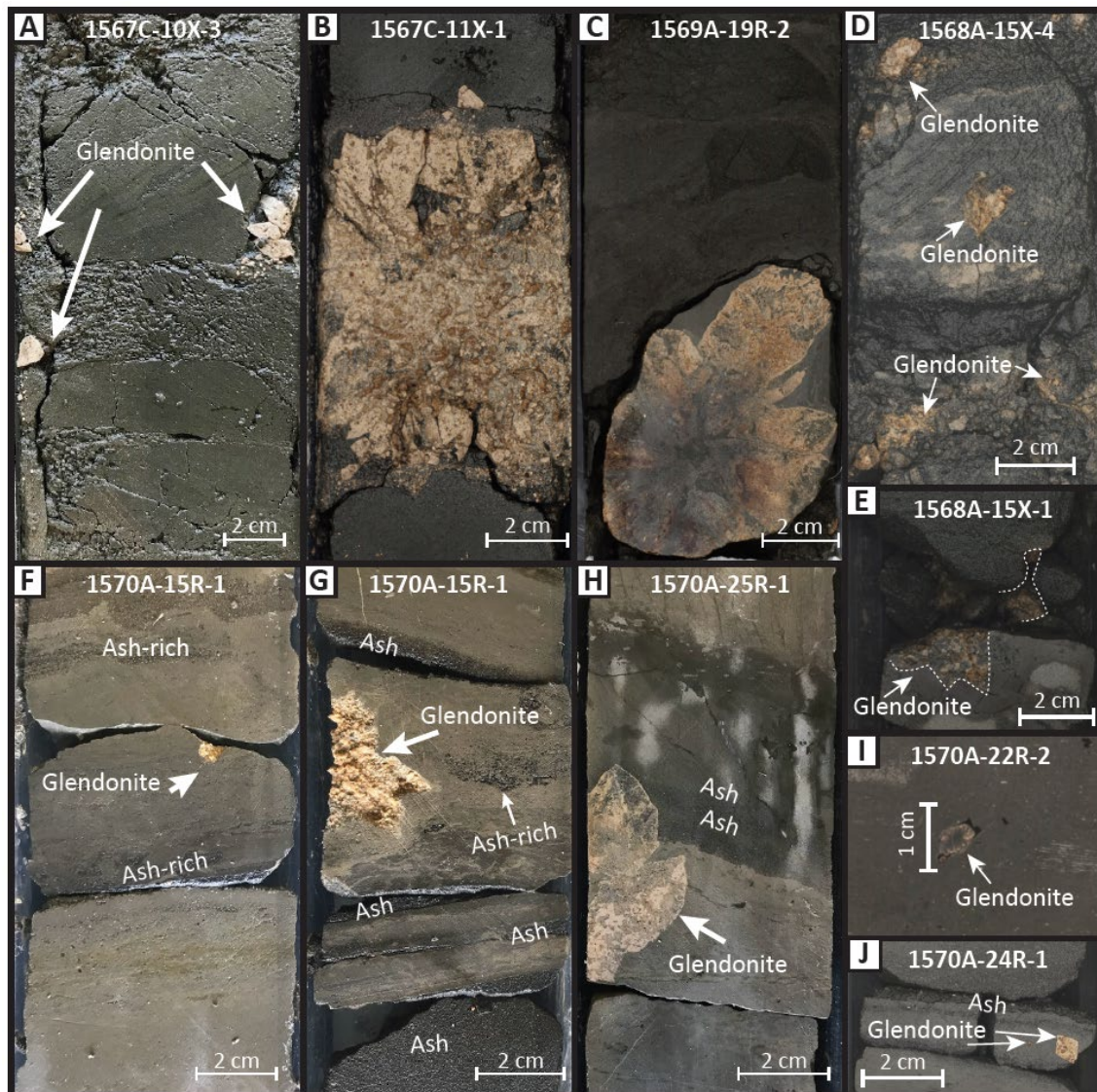


Figure 3: Photographs of glendonites *in situ* in the cores from the Modgunn and Mimir transects. **(A)** Glendonite fragments in drill mud from 1567C-10X-3 40-45 (MLV 86). **(B)** Glendonite from section 1567C-11X-1 94-95 (MLV 57, 97). **(C)** Cemented glendonite from section 1569A-19R-2 54-62 (MLV 90). **(D)** Porous carbonate mush interpreted as glendonite from section 1568A-15X-4 (MLV 88). **(E)** Porous cemented glendonite incorporating host sediment from section 1568A-15X-1. **(F)** Glendonite from section 1570A-15R-1 108-112 (MLV 92). **(G)** Glendonite fragment in 1570A-15R-1 22-25 (MLV 91). **(H)** Glendonite from section 1570A-25R-1 (MLV 93). **(I)** Small cemented glendonite fragment from section 1570A-22R-2. **(J)** *In situ* fragment of glendonite from section 1570A-24R-1.

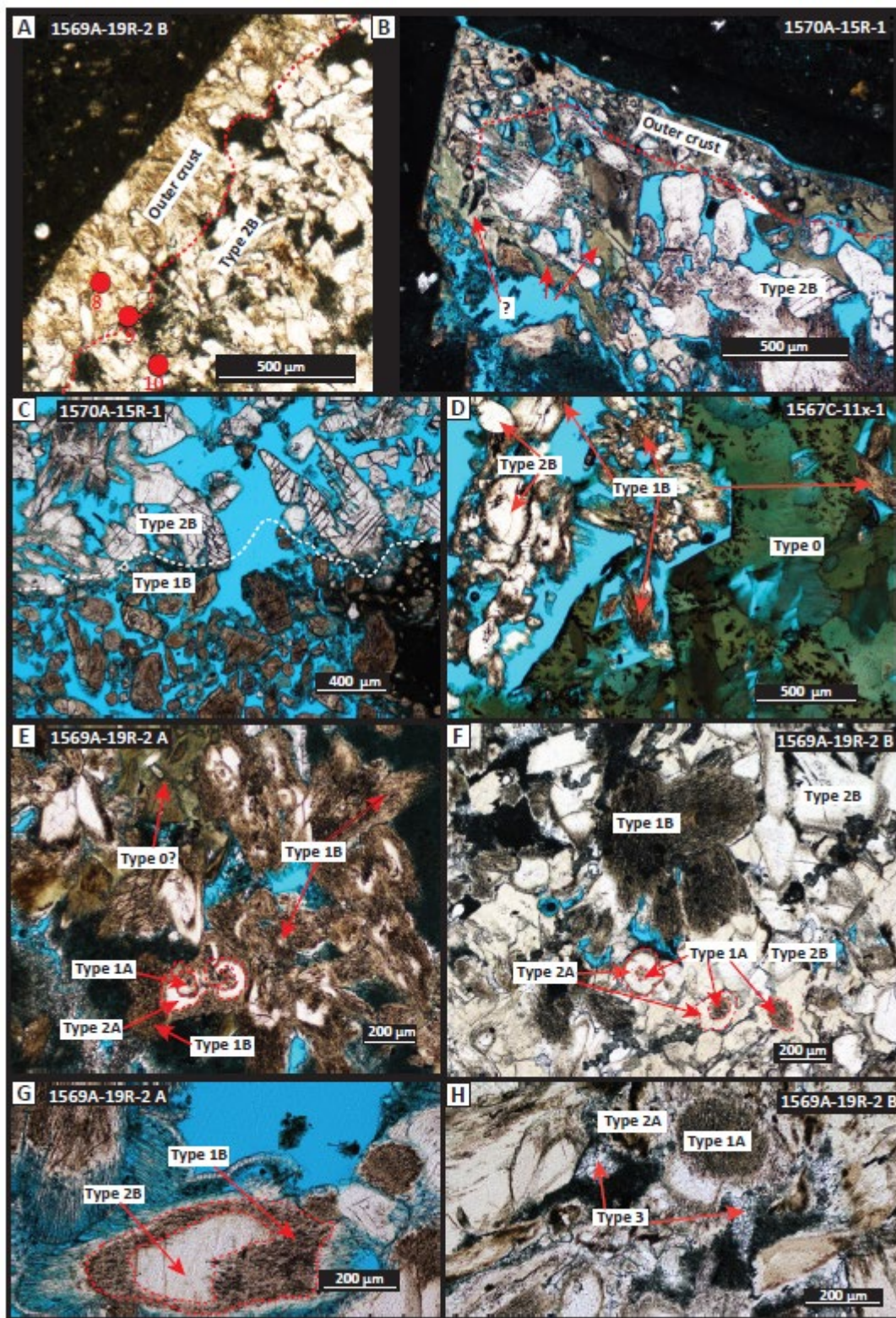


Figure 4: Photomicrographs of polished thin sections from selected Exp. 396 glendonites. The blue background colour is derived from the resin rather than the glendonite. **(A)** and **(B)** show the typical harder outer rim with more porous centre characteristic of transformed ikaite (e.g. Schultz et al., 2023). Red dots labelled 8, 9 and 10 are spots where LA ICP-MS analysis was performed. The glendonites commonly show areas of different calcite types defined by colour, which are often hard to place into the “traditional” carbonate phase types seen in other glendonites (e.g. Huggett et al., 2005; Vickers et al., 2018). **(C)** shows a distinct boundary between white Type 2B calcite and brown Type 1B calcite, neither of which show zoning defined by colour or porosity. **(D)** shows the sharp boundary between green Type 0 carbonate, with black dendritic surface growth, and other calcite phases. The shape of the sharp boundary that Type 0 defines on one side suggests that Type 0 grew on the surface of and out from an ikaite crystal, which later broke down to leave void space and patches of Type 1B with 2B overgrowths. **(E)** and **(F)** show patches of more typical zoned calcite blebs, here labelled 1A and 2A, which appear to fit into the traditional categories of “Type I” (zoned brown calcite forming the centre of the blebs) and “Type II” (zoned pale overgrowths on Type I; e.g. Vickers et al., 2018; Schultz et al., 2023). **(G)** Apparent reversal of the “typical” glendonite fabric, whereby the central area of the calcite blebs is pale/white Type 2B and the overgrowth brown Type 1B calcite. This contrasts with **(H)** which shows dark Type 1A with white Type 2A overgrowths.

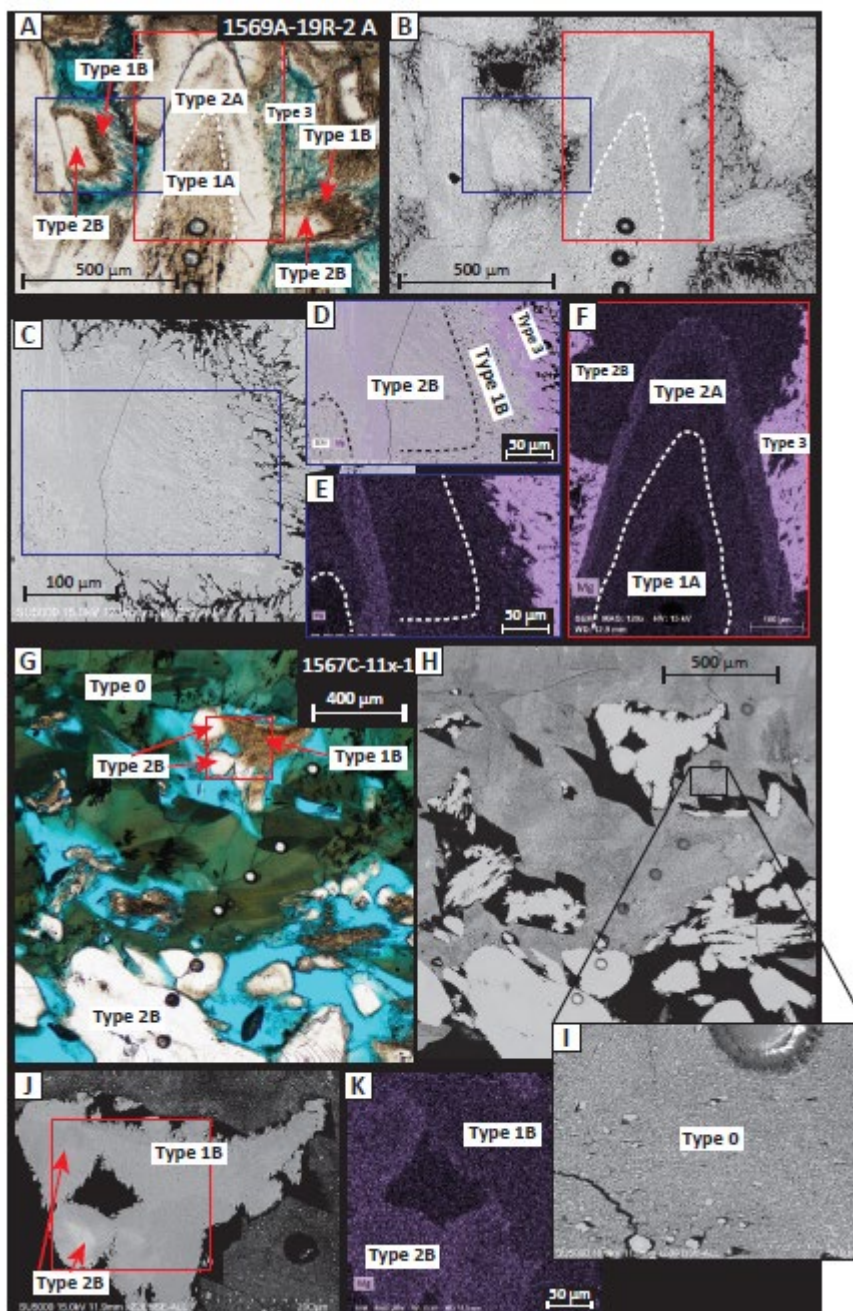


Figure 5: Light microscopy, SEM photomicrographs and EDS element maps from thin sections of glendonites at 1569A-19R-2 and 1567C-11X-1. **(A)** Overview under plane polarised light of the area examined for glendonite at 1569A-19R-2, with the carbonate phases labelled. **(B)** BSE image of the same area. Higher porosity in the Type 1 can be seen. **(C)** BSE image of zoomed in area of Type 2B with Type 1B overgrowth. Higher porosity of Type 1 is again clear. **(D)** EDS map showing Mg distribution across calcite types 1B and 2B, overlaid on the BSE photomicrograph. **(E)** The same map without the BSE photomicrograph **(F)** EDS map showing Mg distribution across calcite types 1A, 2A and 2B. **(G)** Overview under plane polarised light of the area examined for glendonite at 1567C-11X-1. **(H)** BSE image of the same area, with pop-out **(I)** showing the microcrystalline nature of Type 0. **(J)** Magnification of the same area with types 1B and 2B calcite under BSE. **(K)** EDS element map showing the Mg distribution across the same area.

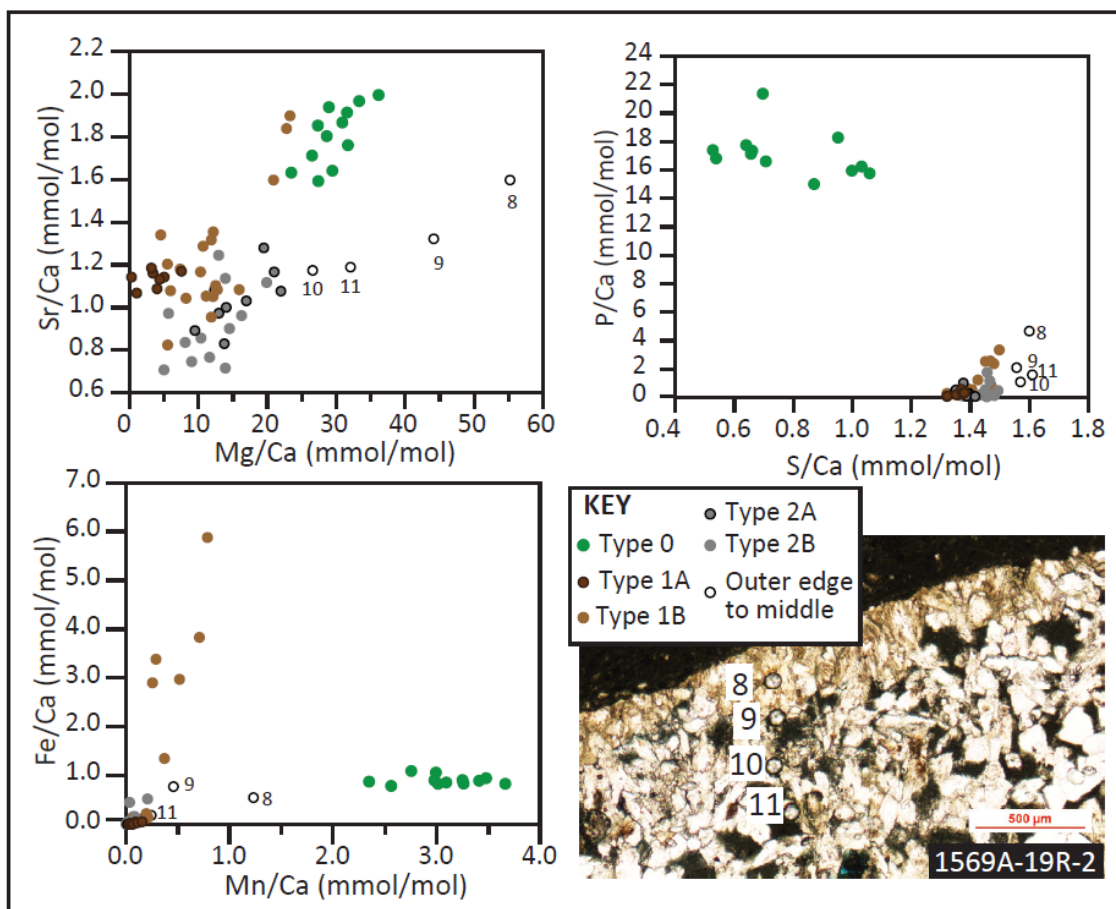


Figure 6: LA ICP-MS element/Ca data for points across the Exp. 396 glendonite polished thin sections. The data have been grouped according to the calcite types described in the main text and in the preceding figures. Photomicrograph showing the location points 8 – 11 from outer edge inwards are shown bottom right, and also in Fig. 4A. Photomicrographs showing the location of all the individual points measured may be found in the Supplementary Material.

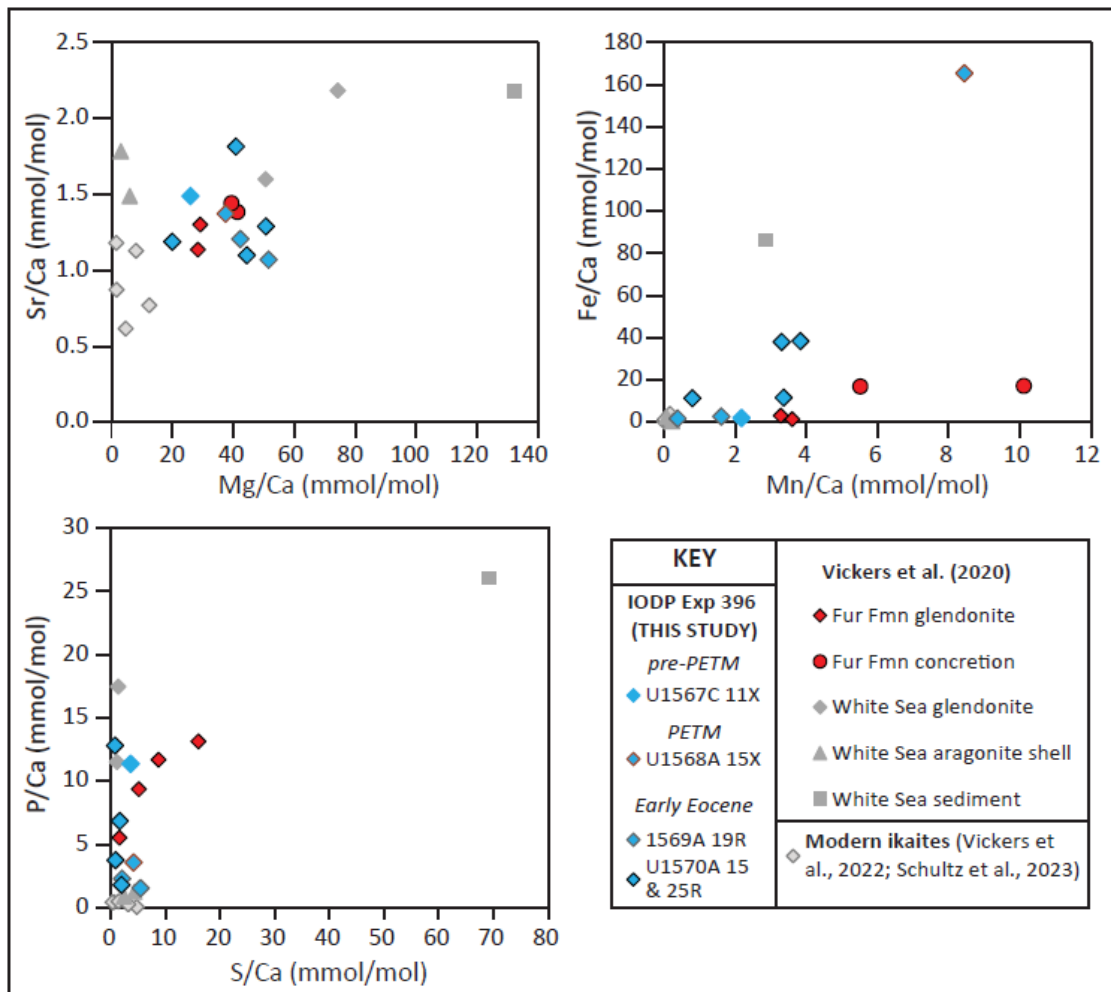


Figure 7: Element/Ca ratios of the Exp. 396 glendonites and associated calcites compared to published ICP-OES data for other glendonite-bearing sites.

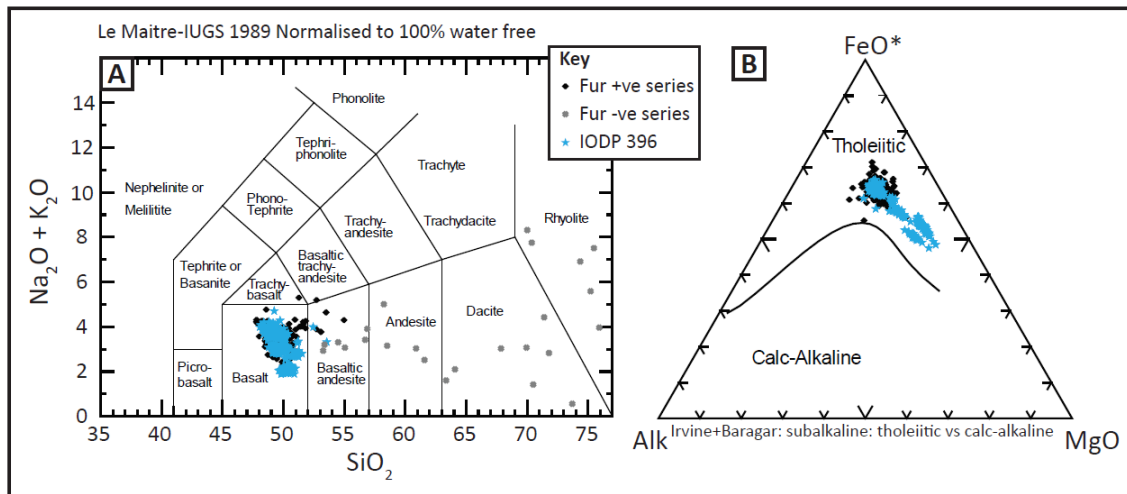


Figure 8: (A) A Total Alkali Silica (TAS) plot comparing the Exp. 396 ashes (this study) to published data for both positive (Stokke et al. 2020b) and negative (Larsen et al., 2003) ash series of the Fur Formation in northern Denmark. The Exp. 396 ashes and Fur positive series fall into the basaltic fields, whereas the Fur negative series show much more variation and have overall more felsic compositions. Note that while the Fur positive series data are microprobe analyses of matrix glass, the Fur Negative series data are whole rock data. However, the whole rock samples were leached of clay prior to analysis and no significant dilution is expected. **(B)** Ternary Alkali-Iron-Magnesium (AFM) diagram showing that the basaltic ashes from both the Exp. 396 sites and the Fur positive series are tholeiitic basalts. Note that many of the Exp. 396 ashes have higher MgO content than the Fur positive ashes.

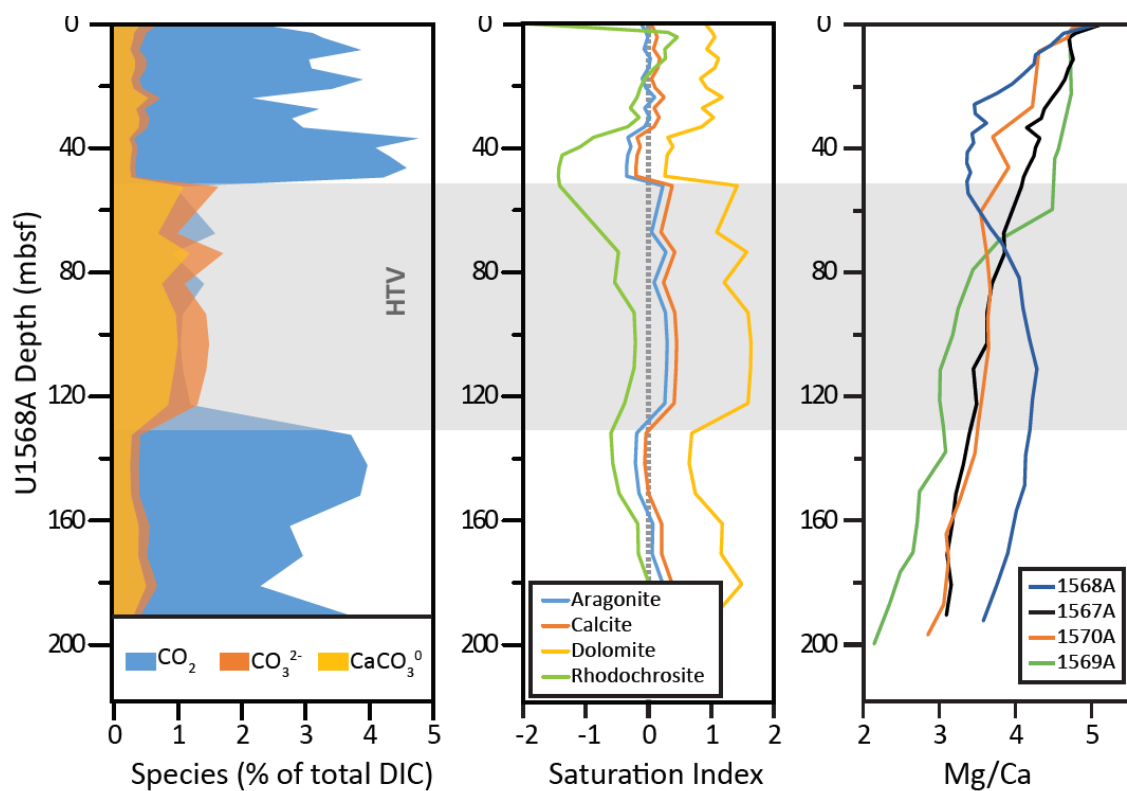


Figure 9: (A) PHREEQC simulation results for carbonate speciation in the U1568A core, which spans the hydrothermal vent infill (grey highlight labelled 'HTV'). Note that HCO_3^- (the major species) is not shown. (B) PHREEQC simulation saturation indices for several carbonate polymorphs. (C) IW Mg/Ca profiles for all glendonite-bearing cores (Planke et al., 2023b,c).

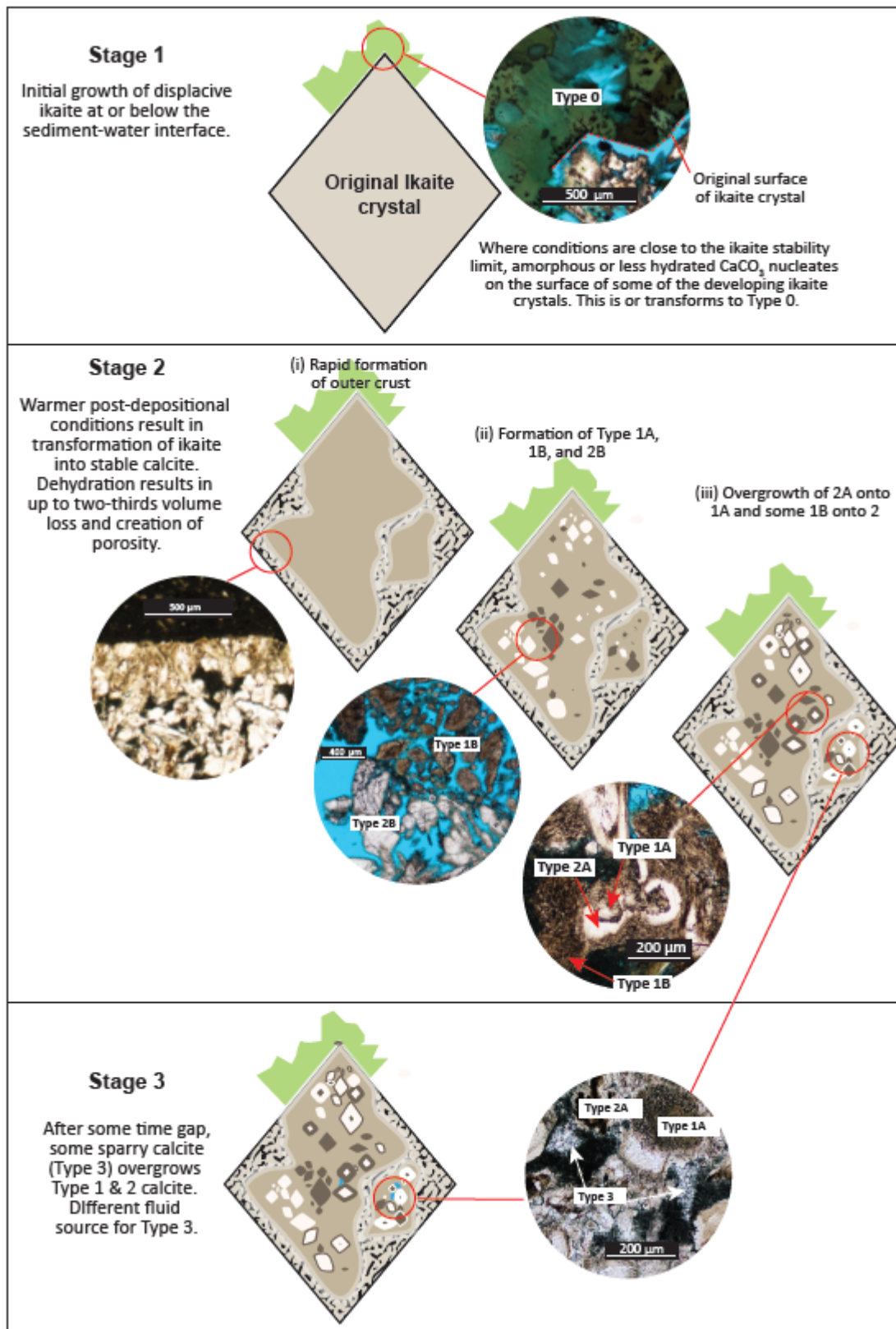


Figure 10: Schematic of ikaite transformation in the Exp. 396 cores, adapted from Counts et al. (*accepted*) based on observed textural relationships and geochemistry of the calcite phases in the Exp. 396 glendonites.

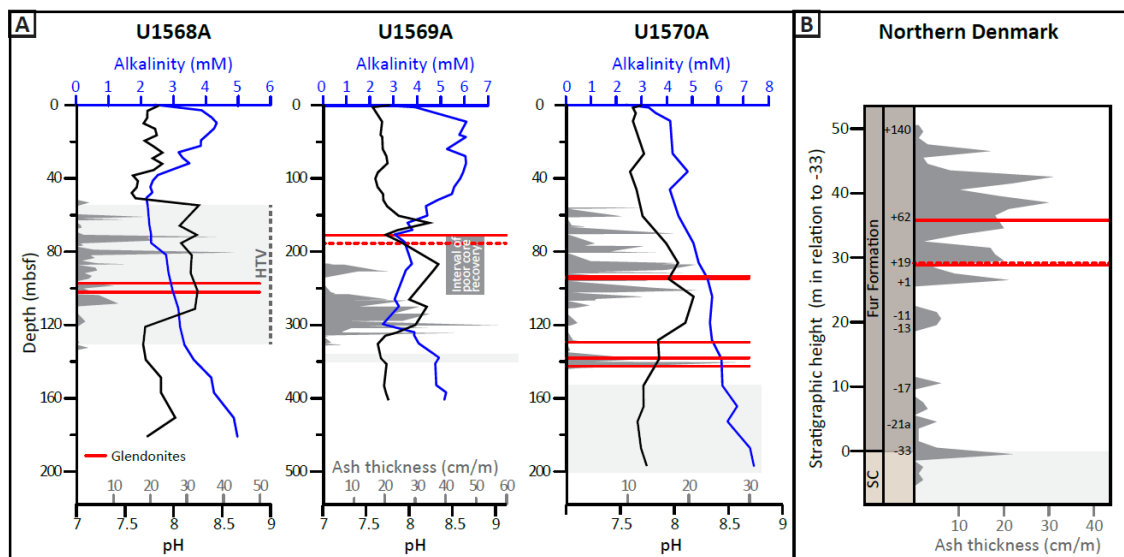


Figure 11: (A) Relative position of glendonites in the Paleocene-Eocene sediments of selected cores from the mid-Norwegian Margin, Exp. 396, compared to measured ash thicknesses. Pore water alkalinity and pH data (Planke et al., 2023) are also shown. Pale grey indicates the PETM-aged intervals in the stratigraphy. Note that for U1569A, core recovery was poor, particularly in the bottom, ash-bearing part (see Fig. 2). High ash contents lead to lower core recovery as they are coarse-grained and unlithified; therefore it is likely that there were much more numerous and thicker ash horizons in the interval between 18R and 37R (c. 180 – 340 mbsf). (B) Relative position of glendonites in the Paleocene-Eocene sediments of Northern Denmark, compared to ash thicknesses per metre (Jones et al., 2023). Glendonite horizons for the Fur Formation are from Vickers et al., (2020) (solid lines) and dashed line as identified by Henrik Friis, pers. comm. Pale grey indicates the end of the body of the PETM carbon isotope excursion (Jones et al., 2023). The recovery phase is between ashes -33 and -21a. SC = Stolleklint Clay.

Site	Hole	Core	Core type	Section	Top depth (cm)	Bottom depth (cm)	mbsf top	PXRD mineralogy	Remarks
1567	C	10	X	3	40	45			Displaced (in drill mud)
1567	C	11	X	1	83	93	82.03	Calcite, minor halite, Qz	Not cemented
1568	A	15	X	1	29	31	97.3		Porous calcite in cement
1568	A	15	X	4	49	51	102.0		Not cemented
1568	A	15	X	4	55	58	102.1	Calcite, minor Qz, rhodochrosite	Not cemented
1569	A	19	R	2	54	62	177.3	Calcite, Mg-calcite, minor Qz, gypsum, halite	Partially cemented
1570	A	15	R	1	22	25	93.6		Not cemented. Small fragment
1570	A	15	R	1	108	112	94.5	Calcite, minor Qz + halite	Not cemented, half glendonite
1570	A	22	R	2	89	91	129.3		Cemented glendonite fragment (tip of crystal)
1570	A	24	R	1	96	98	138.1		Uncemented glendonite fragments
1570	A	25	R	1	50	55	142.5	Calcite, minor Mg-calcite, Qz	Cemented (in lmst)

Table 1: Glendonites of the Exp. 396 cores, PXRD data from bulk glendonite analysis, element/Ca ratios.

Carbonate phase	Description
Type 0	Green-brown, microcrystalline, granular carbonate phase, not observed in all glendonites (Fig. 4). Heterogeneous colour distribution from browner to greener areas, not visibly zoned under plane polarised light (Fig. 4B and F). Commonly shows black dendritic surface patterns. SEM imaging revealed Type 0 to be composed of micro-grains of carbonate, rather than being a single crystal (Fig. 5).
Type 1A	Forms dark and light brown zoned, rounded anhedral patches known as 'blebs' (Figs. 4E,F,H and 5A). The BSE SEM shows it has higher porosity than the calcite overgrowths (Fig. 5B), and EDS mapping shows some chemical zoning defined by its Mg concentration (Fig. 5F). Equivalent to Type 1 (I) of Huggett et al. (2005), Vickers et al. (2018), Schultz et al. (2023), and Counts et al. (2023).
Type 1B	Uneven coloured anhedral brown to dark brown calcite. May radially overgrow, or intergrow with, pale, non-porous Type 2A. Type 1B is indistinguishable from Type 1A except that it grows over Type 2A rather than the other way around, and generally has slightly higher [Mg] than 1A. Type 1B is not visibly zoned, and makes up larger patches/areas (Fig. 4 C – F; Fig. 5). May show cracking along cleavage planes (Fig. 4C).
Type 2A	White to pale brown, concentrically zoned calcite (under plane polarised light) that directly overgrows Type 1A, showing Mg-zoning (Fig. 4), and generally higher Mg than Type 1A (Fig. 5). Low/no porosity compared to Type 1A&B (Fig. 5). Equivalent to Type 2 (II) of Huggett et al. (2005), Vickers et al. (2018) and Schultz et al. (2023) and Type 2A of Counts et al. (2023).
Type 2B	Very similar to Type 2A; clear/white crystalline calcite with no porosity zoning. Unlike 2A, it also lacks chemical zoning, and may show cracks along cleavage (Fig. 5). Type 2B calcite is generally characterised by a higher Mg than Type 1A&B calcite phases (Fig 5).
Type 3	Isopachous sparry or fibrous epitaxial calcite overgrowths to Types 1 and 2; higher [Mg] than types 1 and 2 (Figs. 4H and 5).

Table 2: Descriptions of the different carbonate phases observed within the glendonites through thin section microscopic and geochemical analysis (light microscopy, SEM, EDS and LA-ICP-MS).